Thesis for the degree of Licentiate of Engineering

Vehicle wakes subject to side wind conditions

MAGNUS URQUHART

Department of Mechanics and Maritime Sciences
CHALMERS UNIVERSITY OF TECHNOLOGY
Göteborg, Sweden 2019

Vehicle wakes subject to side wind conditions
MAGNUS URQUHART

THESIS FOR LICENTIATE OF ENGINEERING no 2019:09
ISSN 1652-8565

Department of Mechanics and Maritime Sciences
Chalmers University of Technology
SE–412 96 Göteborg
Sweden
Telephone: +46 (0)31–772 1000

Cover:
Schematic illustration of wake structure between two configurations subjected to side wind.

Chalmers Reproservice
Göteborg, Sweden 2019

"In my experience, there's no such thing as luck" - Obi-Wan Kenobi

Vehicle wakes subject to side wind conditions

Magnus Urquhart
Department of Mechanics and Maritime Sciences
Chalmers University of Technology

Abstract

Passenger vehicles are associated with travel flexibility, today it is clear that this flexibility impacts the environment. Passenger vehicles account for more than one-tenth of all greenhouse gasses in Europe with approximately a quarter of the vehicle's energy consumption wasted as aerodynamic drag. Drag reduction has been and continues to be an active topic impacting fuel efficiency and electric vehicle range. This thesis is on aerodynamic drag of passenger vehicles in side wind conditions. The goal is to increase the knowledge of how vortical structures near the wake relate to the base pressure. The presented work is focused on vehicle wakes and optimisation with the aim to aid in the design of future energy efficient vehicles.

Vehicle wakes are often studied by comparing different configurations. The number of designs and possible combinations to be investigated is often limited due to time constraints. Instead of limiting the possible designs, optimisation was used to aid in the development of a low-drag reference geometry. A surrogate model-based optimisation method was developed and benchmarked against other common techniques. The surrogate model featured adaptively scaled Radial Basis Functions which performed well for the tested benchmark problems. The developed algorithm was used to optimise the geometry at the rear of a vehicle at yaw. This resulted in unexpected designs with good performance.

The investigated geometries featured a base cavity with small angled surfaces, or kicks, at the trailing edge. This kick angle altered the wake balance, reducing the sensitivity to side wind. The wake's unsteady behaviour changed when altering the cavity. Based on the results, it was not possible to find a consistent trend of the unsteadiness of the wake and its relation to drag alone. The results indicate that the improvements to the base pressure were primarily a result of altering the wake balance. The wake balance proved to be the most reliable indicator of drag, with and without additional side wind.

Keywords: aerodynamics, drag, wake, side wind, wind averaged drag, real world conditions, cycle averaged, cavity, tapered extensions, optimization, surrogate model, Radial Basis Functions, Proper Orthogonal Decomposition, Latin Hypercube Sampling

Acknowledgements

First I would like to thank my main supervisor Prof. Simone Sebben for all the support and help I've received in order to improve the quality of my work. I would also like to thank Prof. Lennart Löfdahl for the discussions we've had and the effort he has put into writing applications for post-graduate level courses. The people at Volvo Car Corporation have all been helpful and have always given support when needed and expressed a great willingness to collaborate. Special notice goes to my supervisors Alexander Broniewicz and Lennert Sterken at Volvo Car Corporation for their direct involvement in my PhD project.

A large portion of this work was made possible thanks to the kind people at Loughborough University. Max Varney prepared and built the geometry, setup wind tunnel experiments as well as helped run the majority of these experiments, despite being in the final stages of his thesis. For his dedication and help, I am very grateful. I would also like to mention Matthew Ward who helped with all the PIV experiments and setup. Finally at Loughborough University, Prof. Martin Passmore for making the research collaboration and use of experimental facilities and equipment possible.

This project would not be possible without the financial support from the Swedish Energy Agency who funded this research within the program of Transport, Energy efficient vehicles. The simulations were performed on the computational cluster at Volvo Car Corporation and resources provided by the Swedish National Infrastructure for Computing (SNIC).

I would like to thank my family and friends for the encouragement I've received to pursue a PhD degree. To my fiancée Sofia, thank you for all the support you have given me in this endeavour, not least by proofreading my work.

Finally, I would like to mention my colleagues and friends at VEAS whom all contribute to the great work environment with lots of nice activities such as barbecues, climbing and the occasional pub visits. A special thanks to Sina for putting in the effort and time to organise a lot of these events. Mentioning VEAS without mentioning Sonja would not do the division justice, you are always there to make sure the division keeps running. Last but not least, I would like to show gratitude to my colleagues and friends for the many great technical discussions and the feedback and support you have given.

Nomenclature

F_{D}	Drag force	[N]
C_{D}	Drag coefficient	[-]
$C_{\mathrm{D\ counts}}$	Drag coefficient in counts, $1C_{\mathrm{D\ count}} = 0.001\ C_{\mathrm{D}}$	[-]
C_{DW}	Wind-averaged drag coefficient	[-]
C_{DWC}	Cycle averaged drag coefficient	[-]
P	Static pressure	[Pa]
C_{P}	Pressure coefficient	[-]
C_{Ptot}	Total pressure coefficient	[-]
$F_{\mathrm{resistive}}$	Total resistive driving force	[N]
$\theta_{\mathrm{incline}}$	Road inclination angle	[rad]
F_{RR}	Rolling resistance	[N]
ξ	Flow variable such as pressure or velocity	[N.A.]
ξ_{∞}	Subscript of freestream flow property ξ	[N.A.]
ξ'	Superscript of fluctuating flow property ξ	[N.A.]
$\overline{\xi}$	Time average of flow property ξ	[N.A.]
V	Velocity	[m/s]
ρ	Density	[kg/m^3]
C_{Courant}	Courant number	[-]
v_{cell}	Cell volume	[m^3]
A_{front}	Projected frontal area	[m^2]
St	Strouhal number	[-]
f	Frequency	[Hz]
y^+	Non-dimensional first cell center height	[-]

ν	Kinematic viscosity	[m^2/s]
μ	Dynamic viscosity	[$kg\,s/m$]
$C_\xi(x_A, x_B)$	Two-point correlation between points x_A and x_B	[N.A.]
$C_\xi^{norm}(x_A, x_B)$	Normalised two-point correlation	[-]
L^2	Euclidean norm	[N.A.]
$\mathbf{X}$	Space and time/design-dependent flow matrix	[N.A.]
a_i	i-th time/design-dependent mode	[N.A.]
Φ_i	i-th POD mode	[N.A.]
$\mathbf{W}$	Cell volume matrix	[m^3]
ξ_{RBF}	Radial Basis Function	[N.A.]
ε	Radial Basis Function width	[N.A.]
w_i	Radial Basis Function weight	[N.A.]
$\mathbf{x}$	Point in design space	[N.A.]
A_{RBF}	Radial Basis Function matrix	[N.A.]
c_j	Axis scaling factor of j-th design dimension	[-]
f_i	Function value at location i	[N.A.]
$\overline{f_i}$	Surrogate model prediction at location i	[N.A.]
β_{roof}	Cavity taper angle on the roof	[°]
β_{sides}	Cavity taper angle on the sides	[°]
$\beta_{\mathrm{diffuser}}$	Cavity taper angle on the diffuser	[°]
α_i	Kick angle for the i-th kick	[°]

Abbreviations

GHG	Greenhouse Gas
NEDC	New European Driving Cycle
WLTP	Worldwide Harmonised Light vehicle Test Procedure
WLTC	Worldwide Harmonized Light vehicle Test Cycle
CFD	Computational Fluid Dynamics
RANS	Reynolds Averaged Navier Stokes
LES	Large Eddy Simulation
IDDES	Improved Delayed Detached Eddy Simulation
POD	Proper Orthogonal Decomposition
LHC	Latin Hypercube
RBF	Radial Basis Function
LOO	Leave-One-Out
SM	Surrogate Model
DE	Differential Evolution
RS	Random Search
NM	Nelder-Mead
MAE	Mean Absolute Error

Thesis

This thesis consists of an extended summary of two papers, listed below, as well as preliminary results from an upcoming publication (not listed).

I. Urquhart M., Sebben S. and Sterken L., *Numerical analysis of a vehicle wake with tapered rear extensions under yaw conditions* In: Journal of Wind Engineering and Industrial Aerodynamics, Volume 179, Pages 308-318, ISSN 0167-6105, 2018, https://doi.org/10.1016/j.jweia.2018.06.001

II. Urquhart M., Ljungskog E. and Sebben S., *Surrogate-based optimisation using adaptively scaled Radial Basis Functions* Under review in: Applied Soft Computing - The Official Journal of the World Federation on Soft Computing (WFSC), Under review since 12/03/2019

Division of work

I. All setup, simulation work and analysis for Paper I was done by Urquhart. The wind tunnel tests used for numerical validation were performed by Dr. Sterken. Urquhart wrote the first manuscript which was discussed, reviewed and revised by all authors.

II. The fluid simulations and benchmarking of the surrogate model was performed by Urquhart. The package for scattered interpolation was created by Ljungskog with functionality added by Urquhart. The code for sampling plan creation, Proper Orthogonal Decomposition and surrogate model creation was written by Urquhart. Planning of the research project, discussion of the results and algorithmic improvements to the surrogate model was jointly performed by Urquhart and Ljungskog. Urquhart wrote the first manuscript which was discussed, reviewed and revised by all authors.

Table of Contents

Part I

Extended summary

Chapter 1

Introduction

This thesis is on passenger vehicle aerodynamics, more specifically concerning energy efficiency under realistic driving conditions. The work is focused on vehicle wakes and optimisation related to side wind conditions.

Personal transportation has long been a cornerstone in society, enabling exploration and increasing the distances at which we have been able to cover when travelling to and from our homes and work. The passenger car has had a central role in the development of personal transportation and has been seen as a symbol of freedom by many. Although, it is clear that the flexibility of travel has come at a cost for the environment.

Passenger vehicles were responsible for around 12 % of all greenhouse gas emission in Europe 2016 [1]. The regulations and targets for greenhouse gas emissions have globally become more strict; meanwhile, the gap between certified emission levels and that experience by the customer has been increasing. Testing flexibilities and non-representative operating conditions have been identified as contributing factors to the increasing gap [2, 3]. Aerodynamically relevant factors such as side wind are not considered in the certification process of vehicles today.

Road vehicles are considered bluff bodies characterised by massively separated wakes dominated by pressure drag. To reduce the pressure drag, attention has mainly been focused on improving the pressure recovery in the base wake to reduce the pressure difference between the front and rear of the vehicle. Vehicle modifications are typically investigated without side wind and there is less information available in the literature on the complete wake flow at yaw.

The study of vehicle aerodynamics in combination with real-world operating conditions is an important step towards increasing robustness, reducing emissions and improving electric vehicle driving range. To aid in this, optimisation routines play an important role, both as a tool in vehicle development and as a means to create low-drag reference geometry. The reference geometry can be used to study the drag reduction mechanisms to inspire future designs. The complex flow that occurs in vehicle wakes remains an extensively researched topic where several quantitative and qualitative measures have been used to increase our understanding of wakes.

1.1 Project objective

The objective of this project is to increase the knowledge of vortical structures and their relation to the vehicle's base pressure. For this, different yaw angles are used to study the coupling between the wake topology and the base pressure operating in side wind conditions. The introduction of vehicle modifications that reduce the sensitivity to side wind and improve the overall efficiency will be investigated.

To facilitate the study of base pressure and surrounding flow features, both numerical and experimental tools will be used in the project. This thesis has so far focused on the study of wake structures and the development of an optimisation method which is used to create low-drag reference geometry.

1.2 Limitations

- Both numerical and experimental resources are limited and thus robustness studies of the developed tools are first hand tested on problems that are less resource intensive.
- There are many factors related to real operating conditions that influence vehicle aerodynamics. In this work it is only side wind that is considered.
- Implementation details of active devices, such as wind sensing and mechanical design, will not be considered.

1.3 Outline

The first part of this thesis provides the context for this work. This is followed by background on vehicle aerodynamics, in particular, realistic operating conditions. The following chapters are centred around each study in this thesis. The chapters introduce additional background and methodology specific to each study complete with results and discussion. Finally, some concluding remarks and possible future work is presented, followed by a summary of the appended papers.

Chapter 2

Background

The environmental aspects of passenger vehicles as well as the aerodynamically relevant factors of real-world operating conditions are introduced in this chapter.

2.1 Environmental aspect

Global warming and other environmental concerns, such as urban air quality, are driving factors in passenger vehicle emission legislation. The transport sector was responsible for 27 % of the total greenhouse gas (GHG) emissions in EU ($C0_2$ equivalent) year 2016, including international aviation and maritime emissions [1]. Passenger cars were the largest contributors to transport related GHG emissions, responsible for 44 % of the sectors total emissions, Figure 2.1. This means that

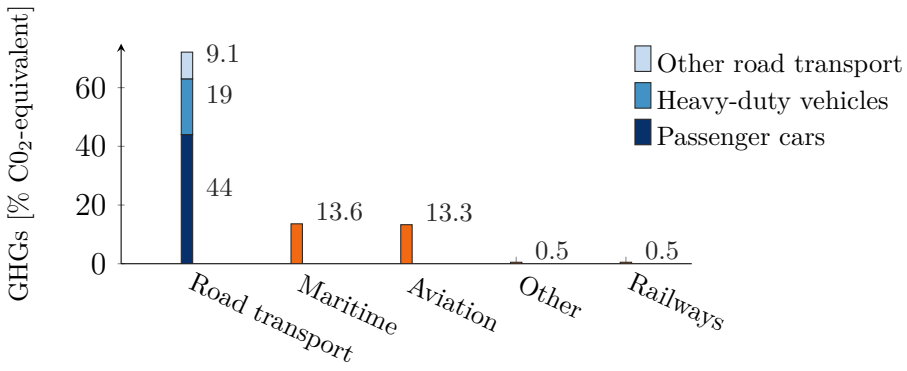

Figure 2.1: *Greenhouse gas emissions within the transportation sector 2016. Data from the European Environment Agency [1].*

passenger vehicles emitted more than 10 % of all GHG emissions in the EU year 2016, which is more than three times that of aviation.

The growing environmental concerns of personal transportation is reflected globally, with an increasing number of countries implementing GHG emission regulations as well as tightening already existing regulations. The historical performance, as well as the enacted and future proposed targets, can be seen in Figure 2.2 [4]. Each country is compared in terms of $gC0_2/km$ normalised to the New European Driving Cycle (NEDC) cycle. Standardised driving cycles are used as a tool by governing bodies to quantify the vehicle performance and enables

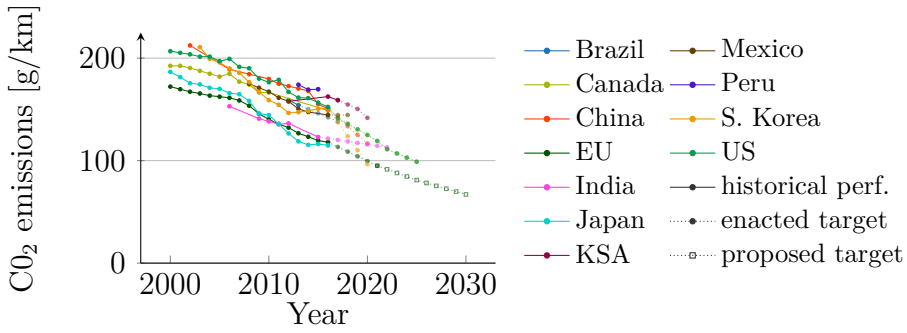

Figure 2.2: *Historical fleet $C0_2$ regulations and current standards normalised to the NEDC cycle for passenger cars, data from The International Council on Clean Transportation [4].*

comparison between different vehicles and manufacturers. The standardised fuel consumption figures can be used by consumers to make informed decisions when purchasing a new vehicle.

2.2 Vehicle testing procedures

Emission targets have been decreasing historically. Meanwhile, the difference between the certified fuel consumption and that reported by consumers has increased, which can be seen in Figure 2.3 [2]. Testing flexibilities have increasingly been

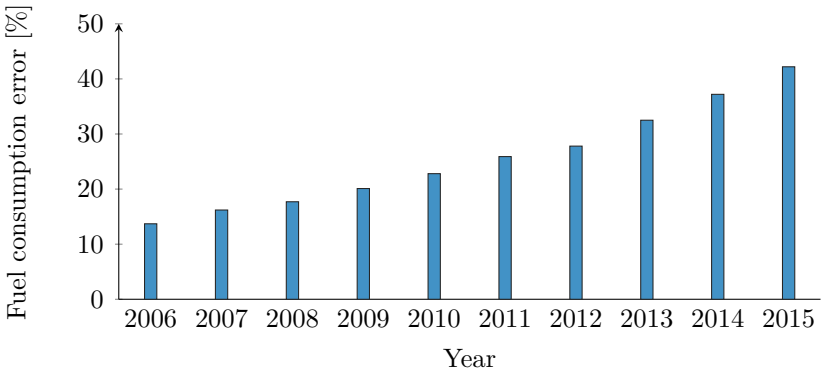

Figure 2.3: *Real-world fuel consumption increase as a percentage of the manufacturer stated fuel consumption using the NEDC testing cycle. Data from the European Federation for Transport and Environment AISBL [2].*

exploited and the vehicles have been optimised for non-representative operating conditions [2, 3]. By 2015 the gap reached 42 %, reducing the intended effectiveness of legislation as well as increasing the incurred fuel cost for the consumers. A quarter of the gap in 2014 was determined to be due to road load determination, where testing flexibilities in the regulated methods such as tire selection, vehicle

preparation and ambient test conditions are influencing factors [3]. Yang et al. [4] stated that the growing gap is a concern, undermining the legitimacy of using standardised testing.

The European Council has implemented a new testing procedure as of 2017 called the Worldwide Harmonised Light vehicle Test Procedure (WLTP). The WLTP aims to reduce the divergence between real-world and advertised fuel consumption performance by reducing testing flexibilities and incorporating new driving cycles which are more representative of real-world use cases. The Worldwide Harmonized Light vehicle Test Cycle (WLTC) relevant for the most commonly sold passenger vehicles, can be seen in Figure 2.4.

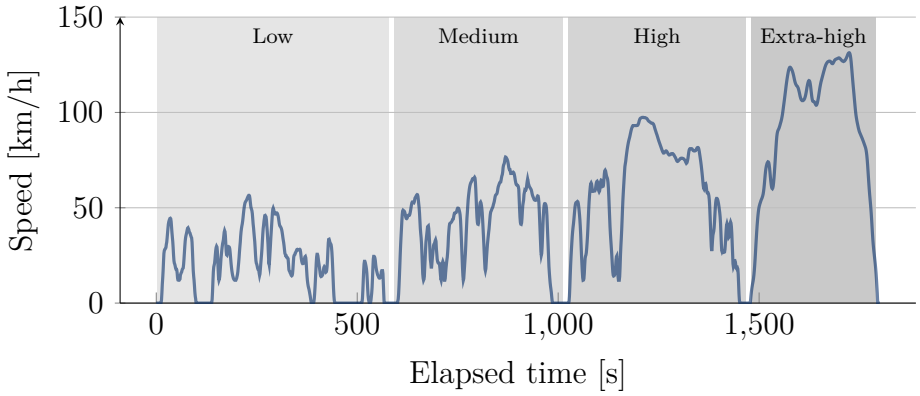

Figure 2.4: *WLTC Class 3 driving cycle.*

The WLTC is split into four phases, Low, Medium, High and Extra-high with several acceleration and braking zones. Aerodynamics is more important in the WLTC, compared to the NEDC, with an increased average speed, from 34 km/h to 46 km/h, and an increased maximum velocity from 120 km/h to 131.3 km/h. Furthermore, the testing flexibilities which influence aerodynamics, such as tested configuration, aerodynamic features and vehicle pre-conditioning, have been reduced in the WLTP. This influences the extent to which vehicle manufacturers can use a energy efficient baseline in the tests which might not be representative of the commonly sold configurations and options bought by consumers.

In a study by Pavlovic et al. [5] 20 petrol vehicles were tested in the WLTC and NEDC. For an average performing vehicle in the high test mass and high road load category, the aerodynamic forces were responsible for 27.6 % of the traction energy required. In the NEDC, using the same vehicle, this number reduces to 23.0 %, highlighting the increased importance of aerodynamics in the more representative WLTC. The trend of increased electrification among passenger cars is another key factor increasing the importance of aerodynamics due to range concerns. Vehicles with the ability to recuperate parts of the kinetic energy during breaking are further positively influenced by improving the aerodynamics due to less kinetic energy being lost as non-recoverable aerodynamic drag during breaking.

According to the report by Tietge et al. [3], the differences between real-world and WLTP-certified fuel consumption is expected to be around 23 % year 2020. This is an improvement over the NEDC which was expected to differ by around 49 % year 2020 in a "business as usual scenario" [3].

2.3 Real-world aerodynamics

The aerodynamic drag is part of the overall driving resistive force, $F_{\text{resistive}}$. The overall resistive force can be split into the force required to accelerate the vehicle, the force due to road incline, the rolling resistance and the aerodynamic drag [6] as,

$$F_{\text{resistive}} = ma + mg\sin\theta_{\text{incline}} + F_{\text{RR}} + F_{\text{D}}. \tag{2.1}$$

Aerodynamic force is often normalised by the freestream dynamic pressure and the vehicle frontal area, e.g. the drag coefficient, C_{D}, becomes

$$C_{\text{D}} = \frac{F_{\text{D}}}{\frac{1}{2}\rho_\infty V_\infty^2 A}. \tag{2.2}$$

It is important to note the square relationship between the aerodynamic force and the velocity. The importance of this is illustrated in Figure 2.5. On a flat road at constant velocity, the aerodynamic drag becomes the dominant resistive force above approximately 70-80 km/h depending on the vehicle. The drag on the

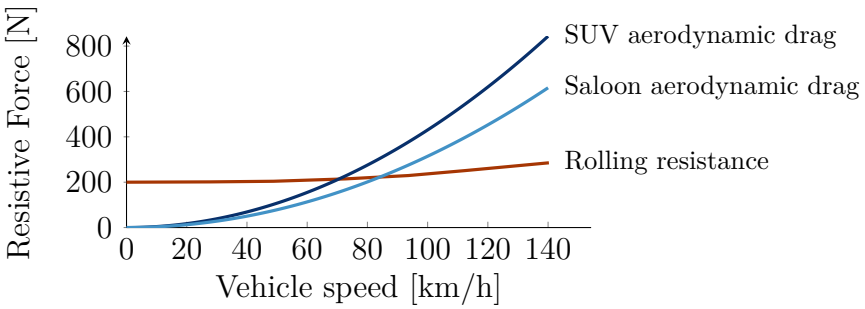

Figure 2.5: *Rolling resistance and aerodynamic drag of a representative SUV and saloon type vehicle. Rolling resistance from [7]. The area and drag for the SUV and Saloon were calculated using the mean area and drag coefficient of the vehicles presented in [8] and [9]. Saloon mean* $C_D = 0.304$*, mean* $A = 2.259$ *and SUV mean* $C_D = 0.358$*, mean* $A = 2.626$*.*

vehicle is composed of pressure and shear forces where the pressure drag accounts for approximately 90 % of the total drag [10]. This is due to road vehicles being short blunt bodies characterised by massively separated wakes.

During vehicle development, it is typical to use a combination of low turbulence wind tunnel test and numerical simulations under constant wind speed and vehicle position. The value of the drag coefficient, C_{D}, is then used as a constant figure for the evaluation of the aerodynamic performance of the vehicle. There are several commonly occurring factors that influence aerodynamics and the value of C_{D}. Examples of such factors are wind, turbulence, cornering, ride height, traffic and tyre pressures. Although the testing flexibilities have been reduced in the WLTP, the aerodynamic drag value is still measured in idealised conditions.

Gaylard et al. [11] showed that the benefit of front wheel deflectors was halved when a high turbulence environment was considered. The reduced effectiveness of the front wheel deflectors under turbulent conditions was attributed to changes downstream of the front wheel. The high turbulence environment removed the beneficial effects in the wake that was observed in the low turbulence testing conditions.

Cornering has also been shown to influence drag with increases of as much as 10 % for corners with a radius of 400m [12]. In the same study by Josefsson et al. [12] left- and right-hand cornering was investigated, revealing differences in drag by as much as 11 % due to underbody asymmetries.

Traffic is another factor which alters the road conditions with aerodynamic relevance. Le Good et al. [13] studied the effects of close proximity platooning on generic vehicles and determined that the effect of following a car closely is dependent on the shape of the involved vehicles. They estimated that fuel savings of more than 30 % is possible with the proper vehicle shape and position. However, increases of more than 10 % in estimated fuel consumption were also found when two individually low-drag vehicles formed a two-car platoon. Thus the aerodynamic low-drag vehicle designs which manufacturers tend toward today, might not be suitable for platooning or operation in close proximity traffic.

Gargoloff et al. [14] investigated the combined effect of on-road turbulence intensity and yaw angle, or side wind. The results from that study showed that realistic flow conditions in strong wind could increase drag by 5 %. Their results indicate synergy effects between the on-road turbulence intensity and the side wind angle. However, the side wind angle was found to be the dominant drag increasing factor.

Favre [15] investigated the effects of a gusty or unsteady side wind event. The unsteady event differed from constant side wind with differences in the vehicle's yaw moment of more than five times larger peak yaw moments for the unsteady event. A generic vehicle with different backlight angles was studied and revealed that the lowest drag configuration without gusts had the largest peak drag values when exiting the gust.

In a study of 51 passenger vehicles of different vehicle types Windsor [8] evaluated the sensitivity of each vehicle to yawed flow. Windsor [8] found that the

drag sensitivity to yaw tended to increase as drag decreased for saloon and sports type vehicles. This indicates that the current methods of optimising vehicles in idealised conditions might be contributing to the increased gap between expected and reported real-world performance.

Wind-averaged drag is an equivalent measure taking into account the wind distribution and, for fixed vehicle speed, gives an indication of the vehicles aerodynamic performance subject to representative wind conditions. It should be noted that the only difference from a regular drag performance figure is the addition of different yaw-angles and that the other previously mentioned influencing factors, such as cornering and on-road turbulence, are not considered when calculating the wind-averaged drag.

Two of the vehicles from the study by Windsor [8] are shown in Figure 2.6 where vehicle B is more sensitive to side wind. Comparing vehicle A and B

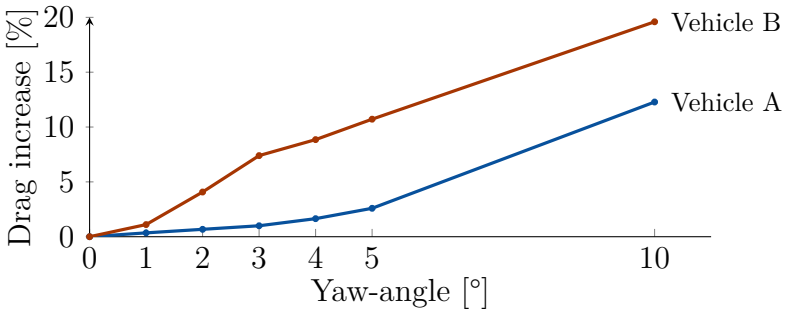

Figure 2.6: *Drag increase per yaw angle for two saloon vehicles. Data from the study by Windsor [8].*

without considering the performance over the entire operating range can result in an unrepresentative performance figure.

Several wind averaging methods exists and are based on wind environment and fixed vehicle speed. Windsor [8] reviewed three methods, MIRA, SAE J1252 and TRRL Report 392 and preferred the MIRA method for calculating the wind-averaged drag. Each method uses yaw data in 15 positions, $\{0°, \pm1°, \pm2°, \pm3°, \pm4°, \pm5°, \pm10°, \pm15°\}$ to calculate the wind-averaged drag. Increasing the vehicle speed reduces the yaw angle experienced for a given wind speed due to the relative motion between the side wind and vehicle. To overcome this, Howell et al. [16] developed the cycle-averaged drag coefficient which takes into account the wind-averaged drag over the entire driving cycle in order to create a representative real-world aerodynamic performance figure. Howell et al. [16] calculated the cycle-averaged drag coefficient (C_{DWC}) for 28 vehicles using the WLTC. Howell et al. [16] found that the typical increase between the drag coefficient at 0°-yaw and C_{DWC} to be 5 %, with the smallest and largest increase being 2.2 % and 11.4 % respectively. To simplify the process of calculating C_{DWC}, Howell et al. [16] estimated the C_{DWC}

using

$$C_{\mathrm{DWC}} = 0.53C_{\mathrm{D0}} + 0.345C_{\mathrm{D5}} + 0.13C_{\mathrm{D10}} + 0.007C_{\mathrm{D15}} \tag{2.3}$$

where the subscript denotes the yaw angle. It was stated that the relative weighting of the terms was found through regression and carries no physical meaning. Howell et al. [16] suggested equation (2.3) be used as an engineering tool to estimate C_{DWC}.

Varney et al. [17] used the cycle-averaged drag proposed by Howell et al. [16] to study asymmetric side tapering. The C_{DWC} was modified by dropping the 15°-yaw term due to its relatively small contribution. Vehicle A, presented in Figure 2.6, has a 3 % increase in C_{DWC} over C_{D0} while Vehicle B has a 7 % increase, using the modified C_{DWC} equation modified by Varney et al. [17]. The C_{DWC} variant using the modification by Varney et al. [17] has been used in this work to estimate the cycle-averaged drag in order to optimise the cavity on a simplified body, as will be discussed later in Chapter 5.

It is clear from the literature that several aerodynamically relevant aspects of the current testing procedures for passenger cars are hindering some of the technical innovations that would facilitate better real-world performance of vehicles today. The heavy vehicle industry has recognised this and employs wind-averaged drag values to a larger extent during development. In the author's opinion, it is not a matter of *if* but *when* more of the aerodynamically influencing aspects are factored into the legislation of passenger vehicle testing.

Chapter 3

Vehicle wake aerodynamics

This chapter covers the main findings in Paper I, as well as providing additional background information on wake aerodynamics.

3.1 Background

The pressure drag is made up of the pressure difference between all the forward and reward facing surfaces and the area that the pressure is acting on. Thus the area and the pressure difference can be reduced to improve the energy efficiency. Historical trends show that the vehicle frontal area has been increasing [18] and due to the spatial requirements for safety, cargo and interior needs, it is often improvements to the pressure difference which is pursued.

Several active and passive methods to increase the base pressure of vehicles can be found in the literature, e.g.: cavities, ventilated cavities, boat tailing flaps, passive bleed, short rear end tapers, vortex generators, splitter plates, synthetic jets, side skirts and blowing techniques [19–28]. The intention of such devices is to increase the base pressure by altering some property of the base flow such as flow direction, balance, wake size and shear layer mixing.

Several quantitative and qualitative indicators have been used in the literature to investigate separated wakes such as shape, size, modal information, closure point location, kinetic energy, turbulent kinetic energy, recirculation angles, vorticity distribution and shear layer growth [23, 29–31]. Altering the wake flow is often linked to changes of several aspects of the wake simultaneously, proving it difficult to separate individual effects of the applied flow control method.

Barros et al. [29] investigated the effects of periodic forcing along the base perimeter of a blunt body. Applying periodic forcing at the natural frequency of the wake was found to increase the momentum entrainment in the wake, reducing the wake length and increasing drag. High-frequency actuation was found to reduce the momentum entrained in the wake, stabilize the wake and provide fluidic boat tailing resulting in a 10 % drag reduction. The simultaneous stabilisation and fluidic boat tailing make it difficult to quantitatively separate the individual contributions.

Perry [32] investigated the wake closure point, size and the kinetic energy within the wake of different geometric variants; however, no clear connection to drag alone was found. Further increasing the difficulty of investigating vehicle

wakes is the trade-off in overall drag and the drag on the base surfaces in separated flow. Ahmed et al. [33] and Howell et al. [34] separately investigated the effect of roof taper angle and found that the drag on the separated base can be increased by increasing the slant angle when the flow is attached over the slant. Contrarily, in the region where the flow is attached over the slant, the drag on the slanted surface increases with increasing angle. Howell et al. [34] found that the resulting effect is a parabolic relationship between drag and slant angle for angles up to 20°.

The complexity of wake flows remains an open topic of research today, however, wake flows have been investigated predominately without side wind. There are several studies where modifications and vehicle shapes have been investigated at yaw, to name a few [8, 9, 15, 17, 21, 32, 35]. While the side wind effects on forces have been studied, there does not appear to be as much material available on the complete wake flow at yaw. This chapter covers the work performed in Paper I, which is a numerical investigation and analysis of the base wake of a fully detailed production vehicle with a tapered 3/4 cavity subject to side wind.

3.2 Methodology

3.2.1 Geometry

The vehicle used in this study is a Volvo XC60 AWD featuring additional underbody panels to improve the flow quality underneath the vehicle and has been used in previous studies [35–37]. The vehicle is fitted with additional tapered 3/4 extensions covering the roof and sides, creating a cavity, Figure 3.1. The taper adds an

Figure 3.1: *Rear view of the smooth extensions, configuration B.*

additional 5° of tapering, compared to the geometry without the cavity, making the total taper angle approximately 15°. The extensions are 150 mm long, where the last 50 mm of the extensions with a kick is aligned with the driving direction, as shown in Figure 3.2. The configurations are referenced as: baseline without extensions, A, smooth extensions, B, and extensions with a kick, C. The vehicle was investigated at 0°-, 5°- and 10°-yaw.

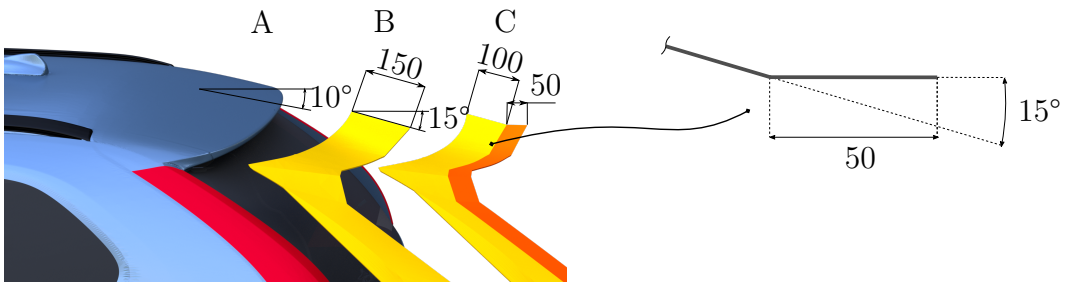

Figure 3.2: *Close-up of the extensions with measurements in [mm]. The taper angle is referenced to the horizontal plane.*

3.2.2 Numerical set-up

The numerical simulations were performed using the commercial Finite Volume Method Computational Fluid Dynamics (CFD) solver Star-CCM+. The turbulence was modelled using a hybrid Reynolds Averaged Navier Stokes (RANS) - Large Eddy Simulation (LES) approach, two equation Improved Delayed Detached Eddy Simulation (IDDES) SST k-ω. A 2^{nd}-order accurate temporal and spatial discretisation scheme was used where the gradients are computed using a hybrid Gauss-Least Squares method. The simulations were run incompressible at 100 km/h, resulting in a Reynolds number of approximately 3×10^6, based on the vehicle length. Unsteady data was saved on the base and on three planes in the wake of the vehicle, Figure 3.3.

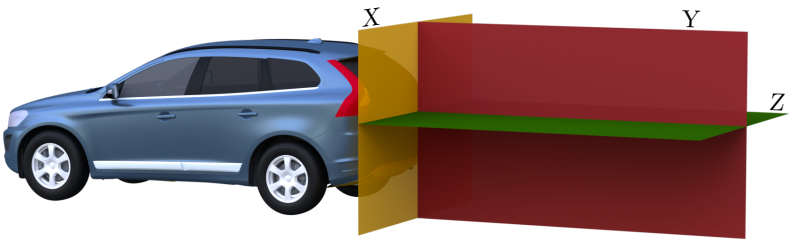

Figure 3.3: *Wake planes where time resolved data is collected.*

The timestep was $2.5 \times 10^{-4} s$, giving an average convective Courant number of 0.9, with more than 70% of the cells being below 1. The Courant number for a cell is defined as $C_{\text{Courant}} = |V|\Delta t / \sqrt[3]{v_{\text{cell}}}$, where Δt and v_{cell} is the timestep and cell volume respectively. The transient data was saved for 12 s for the 0°- and 5°-yaw cases to capture a sufficient amount of low-frequency events to be used in the temporal post-processing. Low frequency events around 1 to 2 Hz or a Strouhal number, $St \approx 0.1$, were expected based on test results from [35], where $St = f\sqrt{A}/V_\infty$.

Approximately 130×10^6 hexahedral dominant cells were used where regions such as the wake shear layer, wheels and the underbody were refined. The majority of the geometry facing the external flow, had 12 prism layers spanning 8 mm with a

first cell height of 0.015 mm resulting in a $y^+ < 1$, as required by the wall treatment. The non-dimensional first cell centre height, y^+, is defined as

$$y^+ = \frac{u_* y}{\nu} \tag{3.1}$$

where y is the cell center height, ν is the kinematic velocity and u_* is the friction velocity, $u_* = \sqrt{\tau_{\text{wall}}/\rho}$, with τ_{wall}, being the wall shear stress.

The computational domain is made to replicate open road conditions with dimensions $18.5l$ long, $4.3l$ tall and $6.5l$ wide with the inlet placed $5.5l$ upstream of the vehicle, where l is the vehicle length, Figure 3.4. Side wind was simulated

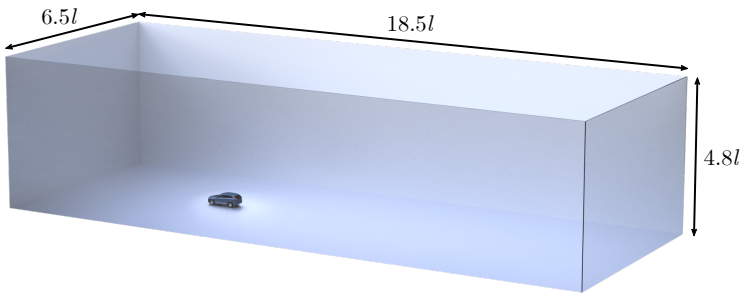

Figure 3.4: *Computational domain.*

by using the left wall of the domain, in the driving direction, as an inlet with the total freestream velocity magnitude being kept constant at 100 km/h to keep the freestream kinetic energy constant.

Mesh- & timestep-evaluation

The influence of the time step was investigated by reducing it to $1.0 \times 10^{-4} s$, showing less than 0.001 ΔC_{D}, or 0.3 % difference in drag between the two timesteps.

The mesh resolution in the separated wake region was evaluated using two-point correlation of the longitudinal velocities. The two-point correlation for a flow variable ξ is expressed as

$$C_\xi(x_A, x_B) = \overline{\boldsymbol{\xi}'(x_A)\boldsymbol{\xi}'(x_B)} \tag{3.2}$$

where x_A and x_B are the spatial coordinates of interest and $\boldsymbol{\xi}'$ is a vector containing the time series of the fluctuating flow variable ξ. Two-point correlation gives a measurement of the temporal correlation between two spatially separated signals and is large and positive for two correlated signals in phase, large and negative for two correlated signals 180° out of phase, and small for uncorrelated signals. A signal correlated with itself is the same as the RMS value of that signal squared. It can be convenient to normalise the two-point correlation to vary between -1 and 1. The normalised two-point correlation reads

$$C_\xi^{norm}(x_A, x_B) = \frac{1}{\boldsymbol{\xi}'_{RMS}(x_A)\boldsymbol{\xi}'_{RMS}(x_B)} \overline{\boldsymbol{\xi}'(x_A)\boldsymbol{\xi}'(x_B)} \tag{3.3}$$

where

$$\boldsymbol{\xi}'_{RMS}(x) = \left(\overline{\boldsymbol{\xi}'^2}\right)^{\frac{1}{2}}. \tag{3.4}$$

According to Davidson [38], the energy spectra, as well as the resolved turbulent kinetic energy ratio, are poor measures of LES resolution. A better alternative was found to be a two-point correlation, where the number of correlated cells gives an indication of the mesh resolution.

A two-point correlation for twenty locations was performed on the centerline plane for the baseline configuration without yaw. The mesh resolution of the centerline plane and three out of the investigated twenty locations can be seen in Figure 3.5. The reference point, x_A in equation (3.3), was taken as the cell

Figure 3.5: *Centerline plane with the positions of three investigated two-point correlation lines.*

located closest to the vehicle body for each line.

Each investigated point showed similar trends as seen in Figure 3.6, with more than twenty cells correlated in the downstream direction.

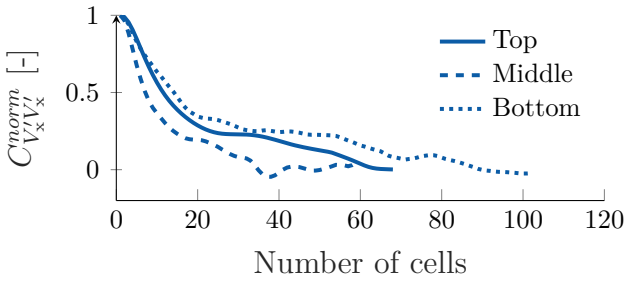

Figure 3.6: *Normalised two-point correlation 100mm behind the vehicle.*

Davidson [38] concluded that coarse LES preferably contained more than eight correlated cells, which was fulfilled for each investigated point. The smallest cells in the wake plane in Figure 3.5 have an edge length of 6 mm.

With this numerical setup, the predicted drag change between configurations is on average within ±2 counts of experiments, with the sign of the predicted trend matching experiments for each configuration. The experimental data is taken from [36].

3.2.3 Post-processing

Local drag

The aerodynamic drag of an object can be calculated by applying the momentum equation to a control volume surrounding the object if the control volume is large enough so that only the wake plane is affected by the object [39]. The time-averaged local drag equation can be stated as

$$\overline{C_{\mathrm{D}}}A = \int_S \left[-\overline{C_{\mathrm{P}}} - 2\left(\frac{\overline{V_x^2}}{\overline{V_\infty^2}} - \frac{\overline{V_x}}{\overline{V_\infty}} \right) \right] dS \tag{3.5}$$

the viscous terms are orders of magnitude smaller than the other terms and have been omitted in this equation. The drag computed by the local drag equation does contain a contribution from the ground which in this case was found to be small, approximately -2 C_{D} counts. The local drag is usually calculated by assuming steady flow [40]; however, neglecting to include the time average of the non-linear terms resulted in an overprediction of drag by as much as 20 % for the vehicle used in this study.

Another form of the wake integral drag, commonly found in the literature, can be calculated by introducing the notion of the total pressure coefficient,

$$C_{\mathrm{Ptot}} = \frac{P + V^2}{\frac{1}{2}\rho V_\infty^2} \tag{3.6}$$

and rearranging the terms in equation (3.5) as,

$$C_D A = \int_S \left[\underbrace{(C_{Ptot_\infty} - C_{Ptot}) - \left(1 - \frac{V_x}{V_\infty}\right)^2}_{\text{Profile drag}} + \underbrace{\left(\frac{V_y^2 + V_z^2}{V_\infty^2} \right)}_{\text{Crossflow drag}} \right] dS. \tag{3.7}$$

Note, the time averaging notation has been dropped in equation (3.7) for convenience.

The last term in the local drag equation, equation (3.7), has been commonly referred to as the lift induced- or vortex drag term; however, Wu [41] recognised that this term is not solely comprised of lift-induced- or vortex drag, since the flow contributing to the third term can exist without causing lift or being part of a vortex. Therefore the last term in eq. (3.7) will hereon be called the crossflow drag. The local drag equation has been used to quantitatively and qualitatively investigate road vehicle wakes by several authors, some examples are [22, 35, 42–47].

Proper Orthogonal Decomposition

Proper Orthogonal Decomposition (POD) is a modal decomposition technique which seeks to find the orthogonal basis vectors that optimally represent the data in a mean squared, or L^2 sense. If the field variable of interest is velocity, this is analogous to capturing the most amount of kinetic energy using the least amount of modes. A brief introduction to the POD technique is given here, more information can be found in the works by Taira et al. [48] and Muld et al. [49].

It is assumed that the flow can be decomposed as

$$\mathbf{X}(\mathbf{r}, t) = \sum_{i=1}^{m} a_i(t)\phi_i(\mathbf{r}) \tag{3.8}$$

where $\phi_i(\mathbf{r})$ is the i-th POD mode and $a_i(t)$ are the time dependent mode coefficients containing the time information. $\mathbf{X}$ is the space and time dependent flow variables arranged as

$$\mathbf{X} = \begin{bmatrix} x_{1,t_1} & x_{1,t_2} & \dots & x_{1,t_m} \\ x_{2,t_1} & x_{2,t_2} & \dots & x_{2,t_m} \\ \vdots & \vdots & \ddots & \vdots \\ x_{n,t_1} & x_{n,t_2} & \dots & x_{n,t_m} \end{bmatrix}$$

with n data points and m snapshots, where one snapshot corresponds to one time step. The matrix $\mathbf{X}$ can also be arranged in terms of space and design configuration, which will be used later in this thesis. The mode coefficients, a_i, are then dependent on the design instead of time. It is possible to find these basis vectors by solving the eigenvalue problem

$$\mathbf{Y}\psi_i = \lambda_i\psi_i, \quad \mathbf{Y} = \mathbf{X}\mathbf{X}^T \tag{3.9}$$

where the modes are calculated as

$$\phi_i = \mathbf{X}\psi_i \frac{1}{\sqrt{\lambda_i}} \tag{3.10}$$

which is often referred to as classical POD. Since $\mathbf{X}\mathbf{X}^T \in \mathbb{R}^{n\times n}$, this can become prohibitively expensive when n is large, as is the case for flow fields. In fluid mechanics, where n is often much larger than m, the method of snapshots is used which solves the eigenvalue problem

$$\mathbf{X}^T\mathbf{X}\psi_i = \lambda_i\psi_i \tag{3.11}$$

which is of size $m \times m$. This formulation assumes the data to be sampled on an equidistant mesh, which seldom holds true in CFD. To use POD on a non-equidistant mesh, the cell volume is included by replacing $\mathbf{X}^T\mathbf{X}$ with $\mathbf{X}^T\mathbf{W}\mathbf{X}$ where $\mathbf{W}$ is a diagonal matrix containing the cell volumes [49]. The mode coefficients $a_i(t)$ are constructed as

$$a_i(t) = \sqrt{\lambda_i}\psi_i^T \tag{3.12}$$

In practice this is often solved using a Singular Value Decomposition (SVD)

$$\mathbf{X} = \mathbf{\Phi \Sigma \Psi}^T \tag{3.13}$$

with the modes $\Phi = \phi_i(\mathbf{r}) = [\phi_1, \phi_2, \dots \phi_m] \in \mathbb{R}^{n \times m}$ and the coefficients $\mathbf{\Sigma \Psi}^T = a_i(t) = [a_1, a_2, \dots a_m] \in \mathbb{R}^{m \times m}$.

Mode convergence

In order to determine if a sufficient amount of transient events are contained in the snapshot matrix $\mathbf{X}$, the snapshot mode convergence was investigated as suggested by Muld et al. [49]. The L^2-norm is used to investigate the convergence of modes and is defined as

$$L^2 = min\left(||\phi_{i,t} - \phi_{i,end}||, ||\phi_{i,t} - (-\phi_{i,end})||\right) \tag{3.14}$$

for the i-th modes where each mode is normalised to length 1 before the comparison. $\phi_{i,end}$ is the i-th mode used for comparison, containing the snapshots for all 12 s. The minimum is used since the sign of each mode is not known. The mode is converged if the L^2-norm approaches 0 before the last snapshot, which by definition is zero. The snapshot convergence for the first 10 modes are presented in Figure 3.7, for the baseline geometry at 0° yaw.

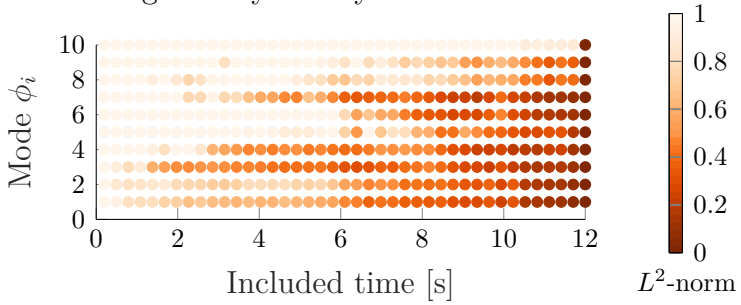

Figure 3.7: *Snapshot mode convergence for the first ten modes.*

The convergence criteria set to the L^2-norm being within 0.1, similar to the work by Muld et al. [49]. The most energetic modes are considered converged after 11 s. Abrupt changes in the modes convergence indicate that the relative placement of the mode has changed; however, this does not necessarily indicate poor mode quality.

In addition to the snapshot mode convergence rate, the sampling rate convergence was also investigated. The sampling rate convergence is computed the same way as for the snapshots, with the difference being the modes $\phi_{i,t}$ now represents modes calculated from a sub-sampled set of $\mathbf{X}$. Each sub-sampled set contains the full 12 s.

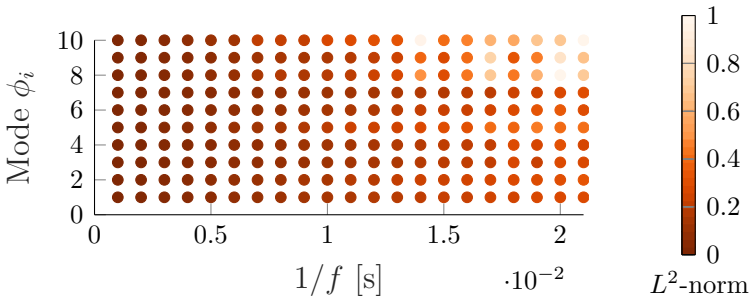

Figure 3.8: *Sampling rate mode convergence for the first ten modes.*

The results in Figure 3.8 indicate that a wavenumber of 0.5×10^{-2}s or, 200 Hz, is a sufficient sampling rate for the L^2-norm of the most energetic modes to be within 0.1. The full sampling rate of 1000 Hz for 12 s was used for all investigations since ample storage and computing power was available.

An additional convergence criterion, which was not investigated here, is the spatial convergence. Each cell in the computational mesh on the sampled surfaces was used for storage. It is possible that a coarser spatial sampling could be used to reduce the storage, memory and computational time needed. Alternatively, the sampled volume could be increased to gain more information for the same cost. ProperOrthogonalDecomposition.jl [50] was used for the POD construction and mode convergence investigation.

3.3 Results and discussion

The 0°-yaw case is presented and discussed first followed by the 5°-yaw case. The results for 2.5°-yaw are similar to the 5°-yaw results and are not shown.

As shown previously by Sterken et al. [35], the kick geometry reduces the sensitivity to yawed flow, Figure 3.9. The lowest drag configuration without side wind is the smooth extensions, B, while at yaw the extensions with a kick, C, provide the greatest drag reduction.

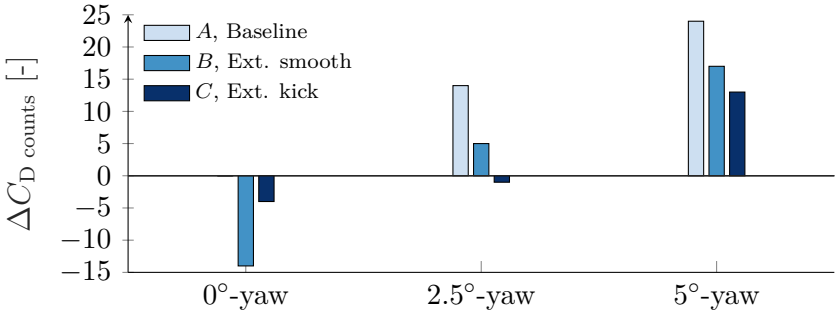

Figure 3.9: *Delta coefficient of drag relative to the baseline.*

3.3.1 0°-yaw

Perry [32] did not find a clear connection between drag and the wake closure point, size and the kinetic energy within the wake. However, the impingement location and the balance of the recirculating region was reported as important factors linked to drag.

In this study it was observed that the impingement location is moved downward for the low drag geometry, configuration B, Figure 3.10.

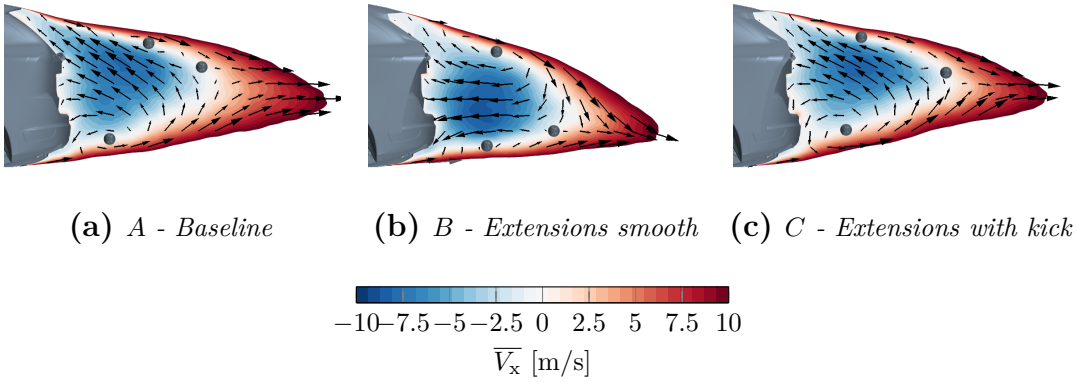

(a) *A - Baseline* **(b)** *B - Extensions smooth* **(c)** *C - Extensions with kick*

Figure 3.10: *Mean longitudinal velocity with velocity vectors. Time averaged singular points are marked with a sphere.*

The recirculating flow vectors for configuration B are angled closer to horizontal and contains larger peak longitudinal velocities. It is believed that the combination of recirculating flow angle and wall-normal velocity magnitude is important to improve base pressure recovery. This is what is referred to as a balanced wake. The improved pressure recovery, as well as the moved impingement location, can be see in Figure 3.11.

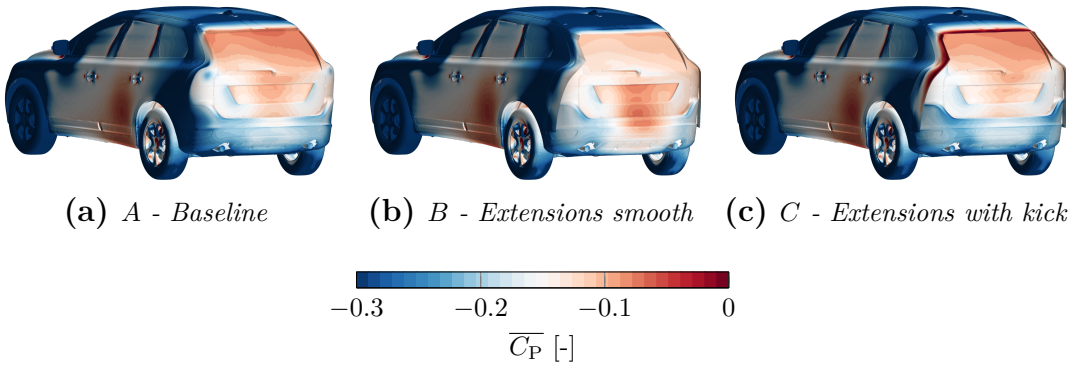

(a) *A - Baseline* **(b)** *B - Extensions smooth* **(c)** *C - Extensions with kick*

Figure 3.11: *Mean surface pressure coefficient.*

The base pressures are qualitatively similar for configurations A and C with the largest differences located at the bumper. The bumper for configuration C sees an increased base pressure compared to the baseline, especially on the sides.

This is likely due to the extensions shielding the lower part of the base from the wheel wake.

The wake plane integral value of crossflow was investigated in several downstream locations using equation (3.7), seen in Figure 3.12. The baseline configuration, A, has the largest peak crossflow value, and is located closer to the base of the vehicle, compared to B and C. The peak crossflow drag locations show no clear correlation with the wake closure points, shown as markers in Figure 3.12. The near wake and peak crossflow drag value are influenced by the kick geometry

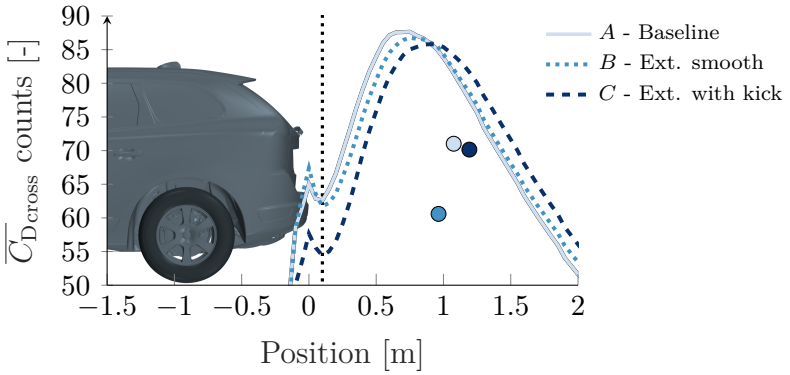

Figure 3.12: *Crossflow drag over X. Marker for wake closure point. Dotted vertical line indicates the* 100 mm *location.*

on configuration C, indicating that the kick re-aligns the flow to the freestream direction. As it will be shown later, this redirection influences the wake shape at yaw, reducing drag.

A two-point correlation was performed for 33 locations distributed across the base where one point was correlated to all other base surface cells. Figure 3.13 shows the two-point correlation for one out of the 33 investigated locations, where the correlated reference, x_A, is illustrated by a yellow sphere. Note that the

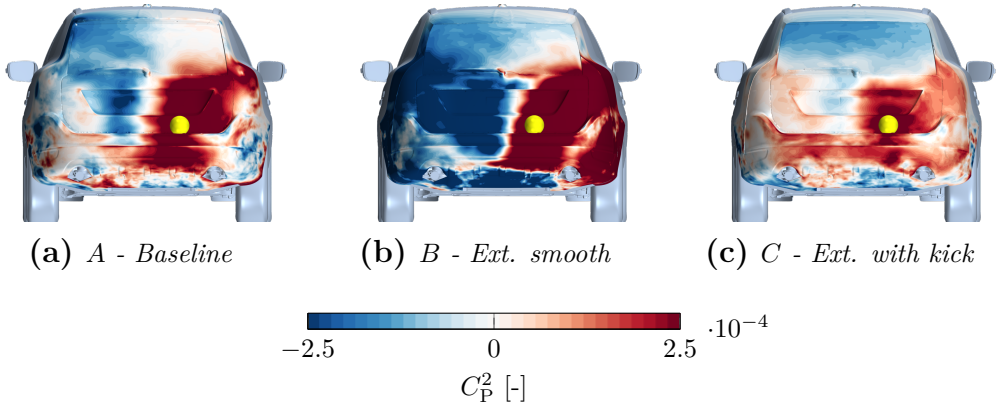

(a) *A - Baseline* **(b)** *B - Ext. smooth* **(c)** *C - Ext. with kick*

Figure 3.13: *Two-point correlation,* $C_{C_P,C_P}(x_A, x_B)$.

two-point correlation is not normalised since the relative magnitudes between

configurations are of interest.

The magnitude of the two-point correlation is large for configuration B with a strong side to side symmetry. The large magnitude of the two-point correlation over the entire base suggests that this is a comparatively strong and coherent wake structure.

The modal information for the three cases was also investigated, Figure 3.14 shows the modal energy for each configuration at 0°-yaw. Configuration C has the most energetic mode corresponding to the top shear layer mode, Figure 3.15. High fluctuating energy in the shear layer is expected to increase entrainment of

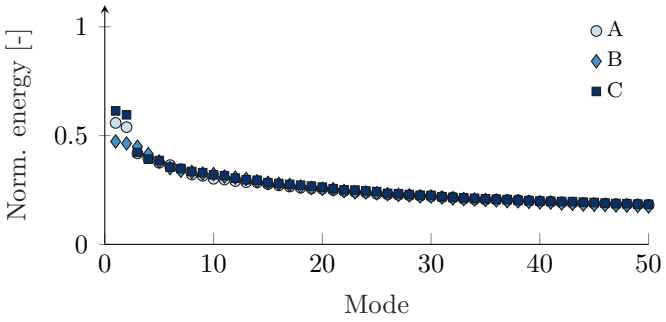

Figure 3.14: *Normalised energy of the 50 largest modes.*

high momentum flow into the wake, shortening the wake and increasing drag [29]. Even though the highest energy shear layer mode is found for configuration C, the drag is lower than for configuration A.

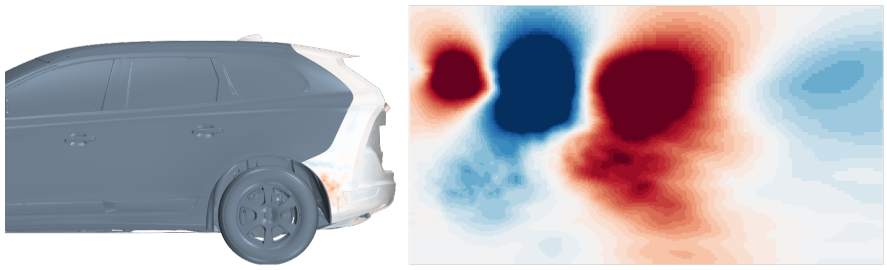

Figure 3.15: *Configuration C. First POD mode, side view.*

It was not always possible to find trends consistent for all the cases. There was often a trade-off between different wake features which hindered the connection between wake features and drag. However, the following observations could be made: (i) Strong shear layer modes alone are not an indication of poor aerodynamic performance. Even though the strong modes suggest that there is potential for further improvement from stabilising the shear layer, reducing entrainment and increasing the wake length [29]. (ii) The results suggest that there is large scale lateral movement from side to side in the wake of configuration B. The anti-symmetric or side to side wake movement has been linked to drag by other authors.

For example, Ahmed [43] showed that the drag on a bluff body could be reduced by placing a vertical splitter plate along the symmetry line to hinder the side to side interaction in the wake. Roshko [51] found that suppressing the periodic vortex formation in the wake of a simple bluff body reduced drag by as much as 30%. While the investigation by Roshko was performed at low Reynolds numbers for a simple body, it indicates that configuration B could be subject to further improvement by hindering the periodic wake movement seen in the antisymmetric modes.

3.3.2 5°-yaw

Since the vehicle is subjected to aerodynamically asymmetrical conditions at yaw, horizontal planes and planes normal to the base of the vehicle are presented for the yawed configurations. The plane in Figure 3.16 is positioned in an area of high return flow velocities, which is located approximately 0.4 vehicles heights from the ground. The lowest drag configuration at yaw, configuration C, is characterised by

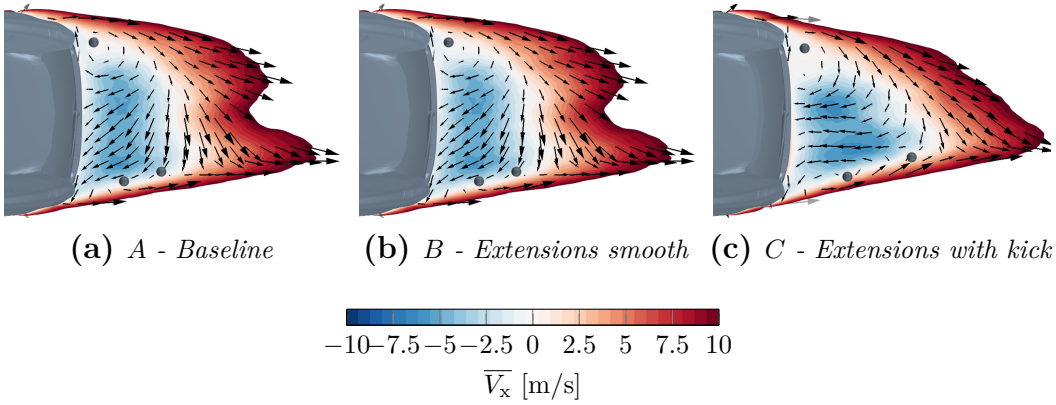

(a) *A - Baseline* **(b)** *B - Extensions smooth* **(c)** *C - Extensions with kick*

Figure 3.16: *Mean longitudinal velocity, top view. Time averaged singular points are marked with a sphere.*

perpendicular recirculating flow, similar to the low drag state at 0° yaw.

A qualitative view of the crossflow drag component reveals the presence of large in plane velocities outlining a large scale twisting motion in the wake for configurations B and C, Figure 3.17. The twisting structure is altered when adding the kick geometry, resulting in lower in plane velocities, increasing base pressure as well as improving the lateral symmetry of the wake. This is illustrated schematically in Figure 3.18 where the large twisting motion is replaced by two smaller structures, improving the wake balance.

The crossflow drag term in the local drag equation, eq. (3.7), can give an indication of potential improvement areas as was seen for the vehicle at yaw. However, when comparing qualitative results, such as Figure 3.17, and integral crossflow drag results, such as Figure 3.12, a consistent correlation to drag could

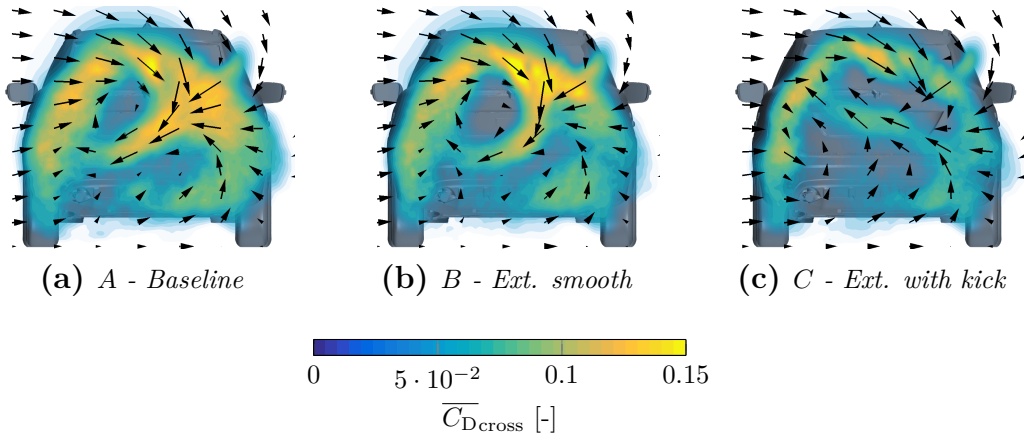

(a) *A - Baseline* **(b)** *B - Ext. smooth* **(c)** *C - Ext. with kick*

Figure 3.17: *Mean crossflow drag with velocity vectors,* 500 mm *behind the vehicle.*

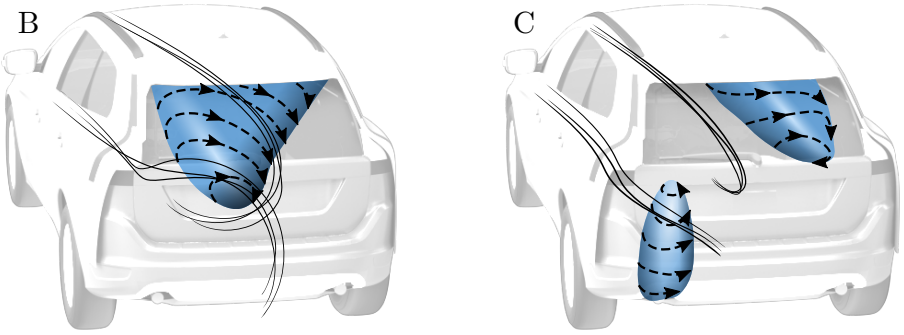

Figure 3.18: *Schematic overview of the wake twisting.*

not be made. Since the drag of the vehicle can be calculated without considering the crossflow components, it is questionable whether it is useful to consider the crossflow drag term as a separate drag contributor for road vehicles.

Kick coverage

The coverage area of the kick was investigated numerically in two additional configurations by applying the kick to the sides only and the roof only. The drag for both configurations was within $\pm 2C_D$ counts of the kick covering the entire $^3/_4$ cavity. Even though the change in drag is small between the different coverage areas, there is a difference in the pressure distribution between the three configurations, Figure 3.19.

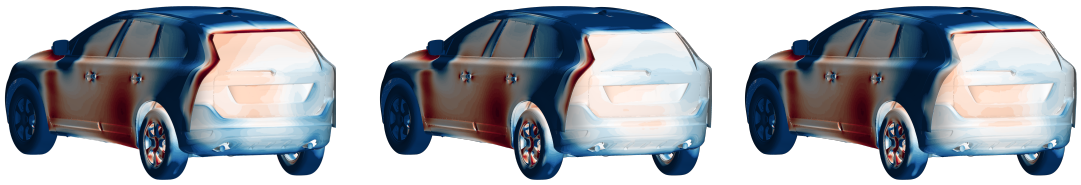

(a) *C - Extensions with kick* **(b)** *Ext. with kick - Only sides* **(c)** *Ext. with kick - Only roof*

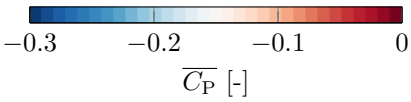

Figure 3.19: *Mean surface pressure coefficient.*

The full coverage kick shows the highest base pressures near the mid and top portions of the wake. Although, this configuration does also have the lowest pressures near the lower portion of the vehicle, balancing the total improvement. The kick applied to the sides only or the roof only results in a more uniform pressure distribution. This raises the question of what the optimal kick coverage is in yawed flow and whether there are other kick angles which would improve the performance further.

Chapter 4

Optimisation

The flow in vehicles wakes is often complex and determining the factors which improve vehicle efficiency is not a trivial task due to complex interactions and trade-offs. The study of vehicle wakes typically involve some geometric change that influences the efficiency of the vehicle which is in turn studied to increase the understanding of the flow physics. Optimisation methods can be used as a tool to aid in the creation of reference geometries.

Optimisation aims to find the best solution to a specific problem and is often bound by some constraints. These constraints are often explicit due to manufacturing or product requirements, but there are also implicit constraints, such as available resources or time budget. Due to implicit constraints, it is not feasible to try all solutions to determine the global optimum, it is thus an improvement over existing designs which is sought after.

When using optimisation tools to improve the geometry, the design space can be explored in an unguided manner. The design is then influenced by the flow psychics rather than human intervention where pre-existing assumptions or knowledge influence the design. Pre-existing assumption and knowledge are still a part of the process since a suitable design space needs to be chosen. During optimisation it is particularly interesting with geometries that influence the performance measure unexpectedly.

This chapter covers the optimisation method development in Paper II, as well as providing additional background information on optimisation.

4.1 Background

The field of optimisation is often split into two categories: gradient-based and gradient-free techniques. Gradient-based optimisation uses the gradient of the objective function to search for better designs. Gradient-based methods perform well for unimodal problems; however, they risk converging to a local optimum if the problems exhibit several minima [52].

Gradient-free optimisation requires no gradient information, as the name implies. The lack of gradient information can increase the number of function evaluations needed to converge compared to gradient-based methods. To combat this problem, the cost of each function evaluation can be reduced, for example by using lower

fidelity simulations or by replacing the physics-based simulations with a data-driven model.

This work focuses on replacing the costly physics-based simulation or physical tests with a surrogate model (SM). The surrogate model is used to find new promising designs and is created from test- or simulation-data. The trade-off when replacing the expensive objective function with a surrogate model is the dependency of the surrogate model's predictive capability, i.e. accuracy, when searching for new designs. The accuracy of the surrogate model typically increases as the number of tests used to create the model increases. Infill strategies where more data is added to the surrogate model are employed to increase the accuracy of the surrogate model while exploring promising designs space. One such strategy was developed by Goel et al. [53], and consisted of an ensemble of surrogates to determine where the differences between the surrogate models in the ensemble was large, in order to find regions of high uncertainty in the design space. They noted that regions where the differences were small did not necessarily correlate with low uncertainty.

Two surrogate models are compared in this work, a POD-based surrogate and a force-based surrogate. The use of POD in optimisation has been investigated by several authors [54–58]. For example, Miretti et al. [56] used a POD-based surrogate model to reduce the number of computations needed by 30 % to 40 % in relation to other gradient-free methods when optimising the drag of a road vehicle.

In a POD-based approach, flow fields are used as the input to the model and a flow field is returned as the output. Since the flow field is given as input to the POD-method, it is suitable for use in simulation work, although flow measurements in a wind tunnel could also be used. The input to the force-based surrogate model is a scalar. In this work the scalar is the drag force but could be any scalar of interest. The output is also a scalar value. This will be referenced to as the force-based approach out of convenience.

The accuracy of the method was evaluated using CFD simulations of the generic vehicle DrivAer, developed by the Technical University of Munich [59]. The DrivAer was investigated using three design variables; roof angle, diffuser height and front wheel deflector on/off. The surrogate model's performance when used in optimisation was benchmarked with nine test functions with and without added noise.

4.2 Methodology

4.2.1 Latin Hypercube Sampling

To create the surrogate model an initial set of samples was used. The locations of the samples were determined using a Latin Hypercube (LHC) sampling plan.

Each design parameter is split into N equally sized intervals where the same value of each design parameter is only allowed to occur once.

Randomly generated LHC sampling plans can suffer from non-uniformly sampled areas, leaving parts of the design space less explored. To improve the distribution of samples, the sampling plan is optimised using the Audze-Eglais objective function

$$\min U = \min \sum_{p=1}^{P} \sum_{q=p+1}^{P} \frac{1}{L_{pq}^2} \tag{4.1}$$

with L_{pq}^2 being the distance between two sample points. The LHC sampling plan is optimised using a permutation genetic algorithm based on the work by J. Bates et al. [60]. Two examples of an optimised and a randomly generate plan can be seen in Figure 4.1b, the optimised plan shown is the plan that was used for the two-dimensional accuracy test case.

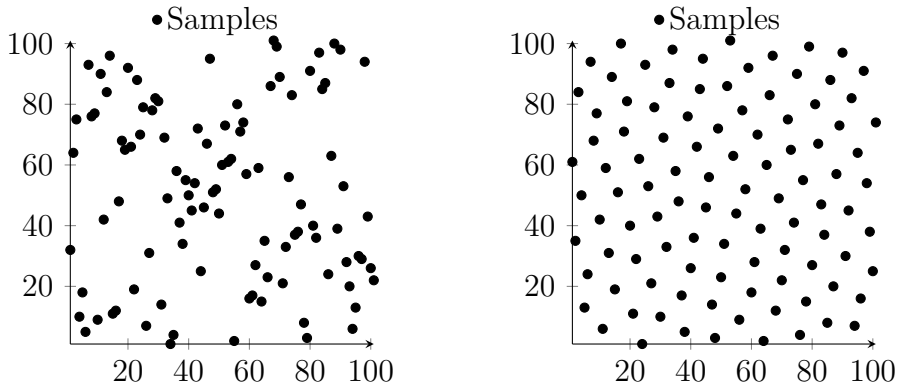

(a) *Randomly generated.*

(b) *Optimised, min. Audze-Eglais objective.*

Figure 4.1: *Two dimensional LHC sampling plans with 101 sample points.*

Categorical Latin Hypercube Sampling

Latin Hypercube sampling plans require an equal amount of points in each design dimension to satisfy the requirements of sampling each design parameter in the same location only once. This limits the use of LHC plans where one or more of the design dimensions is categorical, such as an on/off variable. A categorical dimension is added to the LHC plan where the same value is allowed to appear multiple times to fill up the categorical dimension. The design dimensions can then be a mix of continuous and categorical, or discrete, design parameters. This is strictly no longer a LHC as the same value for a design parameter is allowed to appear multiple times in the categorical dimensions.

To optimise the categorical LHC, the objective function is altered by including the Audze-Eglais objective within each plane. This promotes separation of the design points in each categorical plane in addition to the separation between each points. Without this modification, there is a risk of the plan being clustered of only one categorical value in areas of the continuous design space.

The effect of different weightings can be seen in Figures 4.2a and 4.2b. It should

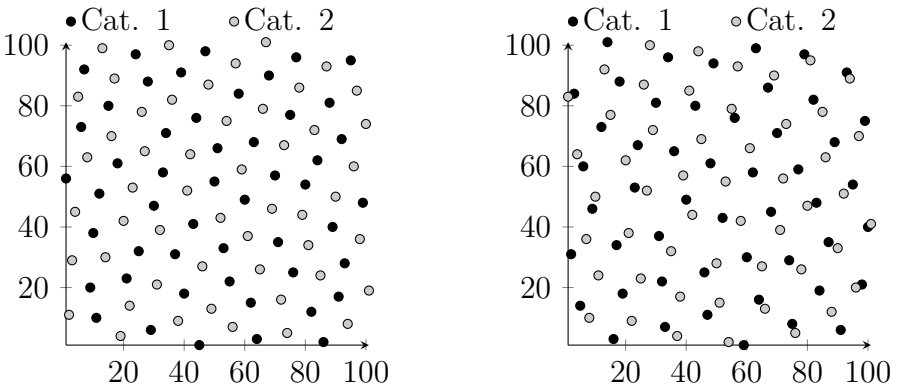

(a) *Continuous* = 0.9975, *Categorical* = 0.0025.

(b) *Continuous* = 0.0025, *Categorical* = 0.9975.

Figure 4.2: *Categorical LHC sampling plans with varying weights of 101 sample points. The two categories are represented by grey and black dots respectively.*

be noted that putting large emphasis on the categorical separation is similar to creating two separate sampling plans. This work uses the weights 0.9975 between all points and 0.0025 for the categorical separation to promote inter-sample separation while punishing clustering of the categorical values.

4.2.2 Radial Basis Function Interpolation

The surrogate model used for optimisation is a Radial Basis Function (RBF) interpolation. For the POD-based surrogate model, new flow fields are created by interpolating the POD coefficients for each POD mode and then reconstructing the flow field using the new coefficients. The RBF interpolation is calculated as

$$u(\mathbf{x}) = \sum_{i=1}^{N} w_i \xi_{\text{RBF } i}(\|\mathbf{x} - \mathbf{x_i}\|_2) \tag{4.2}$$

where w_i are the weights and $\xi_{\text{RBF } i}$ is the Radial Basis Function, and $\|\mathbf{x} - \mathbf{x_i}\|_2$ denotes the euclidean distance between the new point $\mathbf{x}$ and a sample point $\mathbf{x_i}$. The RBFs, $\xi_{\text{RBF } i}$, used in this work are the gaussian,

$$e^{-(\varepsilon r)^2}, \tag{4.3}$$

inverse quadratic,

$$\frac{1}{1+(\varepsilon r)^2}, \tag{4.4}$$

and inverse multiquadratic

$$\frac{1}{\sqrt{1+(\varepsilon r)^2}} \tag{4.5}$$

basis functions where ε is the width factor determining the size of the RBF. An example of the influence of the width factor can be seen in Figure 4.3.

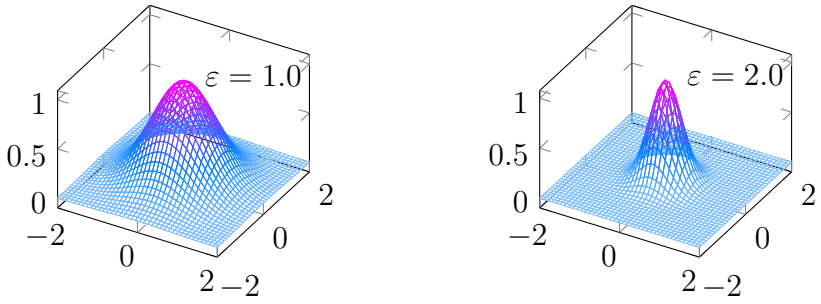

Figure 4.3: *Gaussian RBF with different width factors, ε.*

The weights w_i are found by solving the linear system

$$\mathbf{A}_{\mathrm{RBF}}\mathbf{w} = \mathbf{u} \tag{4.6}$$

where $\mathbf{A}_{\mathrm{RBF}} = A_{ij} = \xi_{\mathrm{RBF}\ i}(\|x_i - x_j\|_2)$, and $\mathbf{u} = \mathbf{u}(\mathbf{x_i})$ is the known function values at the sample points.

Radial Basis Function hyperparameter optimisation

The hyperparameter tuning of $\xi_{\mathrm{RBF}\ i}$ and ε_i was done with the Differential Evolution (DE) algorithm de/rand/1/bin/radiuslimited with a population size of 50, crossover probability of 0.7 and differential weighting factor of 0.6. The objective function to improve the interpolant was the Leave-One-Out (LOO) cross-validation error. The interpolant was created from $n-1$ points and the prediction for the removed point was compared to its actual value to find the error, e_i, at location i. This process was repeated for all n points and the LOO RMS error

$$E_{RMS,LOO} = \sqrt{\overline{\mathbf{e}^2}} \tag{4.7}$$

was used to quantify the performance of the interpolants. The LOO error for all n points is expensive to calculate, but thanks to Rippas algorithm [61], the LOO error can be estimated without computing the solution to equation (4.6) n times. The computational complexity was reduced one order to $\mathcal{O}(n^3)$ using Rippas algorithm.

Dimension scaling

The design parameters used to construct the surrogate model were in the form of engineering quantities. For surrogate modelling, the design dimensions are typically scaled from 0 to 1 or used directly without modification, which can pose a problem due to RBFs being radial. This is illustrated using the three-hump camel function

$$f(x, y) = 2x^2 - 1.05x^4 + \frac{x^6}{6} + xy + y^2 \tag{4.8}$$

in the interval $[-5, 5]$ for both dimensions. The function, Figure 4.4, features large changes in one of the dimensions and relatively small changes in the other. When

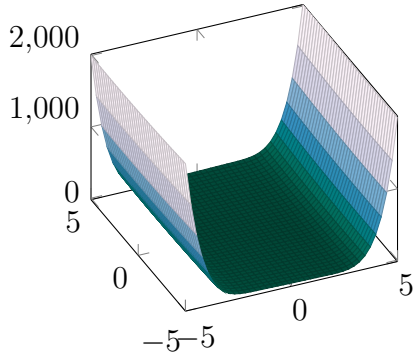

Figure 4.4: *Three camel hump function.*

optimising the interpolant, all dimensions are considered equally important which leads to a compromise of selecting the RBFs, $\xi_{\text{RBF}\,i}$, and the widths, ε_i, which best fit the entire function shape. To improve the RBF interpolation fit when dimensions of differing scale are used, a dimension scaling factor c_j was used, as

$$x_{i,scaled} = c_j \frac{x_i - \min(x)}{\max(x) - \min(x)} \tag{4.9}$$

where $c_j = [c_1, c_2, ..., c_d]$ and d is the number of design dimensions.

This influence of scaling can be seen in Figure 4.5 where three variants, with varying degrees of freedom, were used to create the surrogate model. The inclusions of adaptive axis scaling improved the interpolants ability to fit the sample data and reduce the global error.

Pratical considerations

Due to finite numerical precision, the condition number of matrix $\mathbf{A}_{\text{RBF}}$ needs to be considered as well as the numerical precision of dimension scaling.

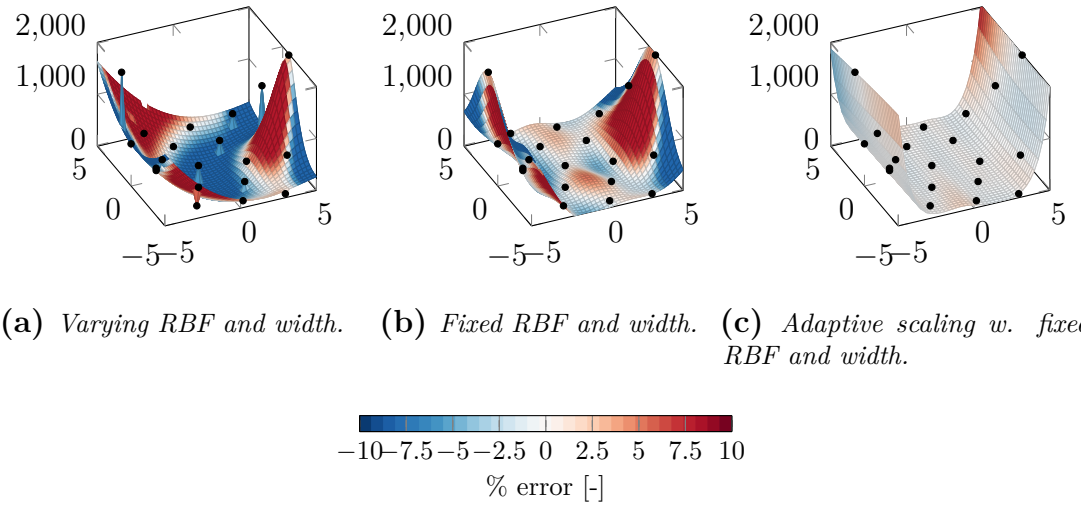

(a) *Varying RBF and width.* **(b)** *Fixed RBF and width.* **(c)** *Adaptive scaling w. fixed RBF and width.*

Figure 4.5: *Interpolation of the three camel hump function. Black markers denote the initial sample points used to create the interpolant.*

When dealing with data containing noise, the RBF interpolation exhibits high-frequency oscillations when the number of interpolation points increases. This is due to the interpolant creating a fit containing the noise as well as the global function shape. Fasshauer [62] suggests using ridge regression when dealing with data containing noise. A regression term, λ, was added to the diagonal of $\mathbf{A}_{\text{RBF}}$, equation (4.6). This term was treated as an additional hyperparameter which was optimised together with the rest of the RBF hyperparameters.

The hyperparameter optimisation is stochastic and therefore yields different solutions each time. To illustrate this, an interpolant based on the Forrester function

$$f(x) = (6x - 2)^2 \sin(12x - 4), \tag{4.10}$$

was recreated 1000 times based on five equidistantly spaced sample points. The average interpolant along with the standard deviation based on the 1000 interpolants can be seen in Figure 4.6. The flexibility of the RBF interpolation can lead

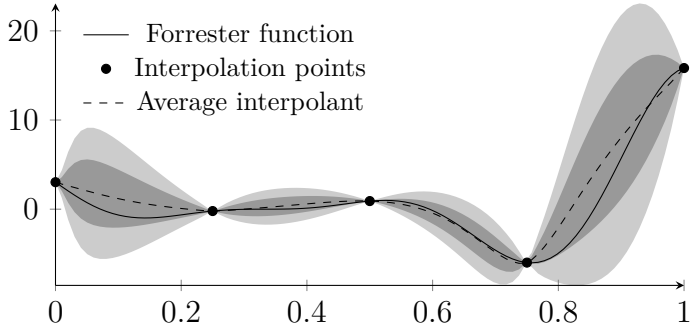

Figure 4.6: *Forrester function and interpolant created from five points. The shaded areas represent the ±1 and ±2 standard deviation of the surrogate model base on 1000 runs.*

to overfitting, where the number of free parameters is large compared to the problem [63]. It is not clear what degree of freedom is suitable and is investigated in the results.

The surrogate model was used to determine the next sample location after each function evaluation. A new sample point was added based on the predicted minimum or the largest standard deviation between an ensemble of surrogates. This strategy was inspired by Goel et al. [53] who used several different surrogates to predict areas with large uncertainty. The ensemble consisted of 20 surrogate models where the prediction was taken as the median value of all surrogates. The infill was carried out in an alternating fashion between the standard deviation of the ensemble and the minimum median ensemble prediction. An example of the infill process is shown for the Forrester function, equation (4.10), in the Appendix, Figure A.1. The POD-based optimisation procedure is outlined in Algorithm 1.

Algorithm 1: POD-based optimisation.

Result: Optimised geometry
Create optimised Latin Hypercube Sampling plan;
Simulate all the designs in the plan;
Interpolate $\mathbf{X}(\mathbf{r}, d)$ to common mesh;
while *within computational budget* **do**
  $\Phi_{n\times m}, A_{m\times m} = \mathbf{POD}(\mathbf{X})$;
  foreach *row in A* **do**
    $\mathbf{RBFinterp} = \mathbf{optimiseRBFinterp}(row)$;
  end
  while *Evolutionary Algorithm* $\neq$ *Converged* **do**
    for $i \leftarrow 1$ **to** m **do**
      $a_{i,new} = \mathbf{RBFinterp}_i(d_{new})$
    end
    $\mathbf{X_{new}}(\mathbf{r}, d_{new}) = \sum_{i=1}^{m} a_i(d_{new})\phi_i(\mathbf{r})$;
    $objective = \mathbf{integrationPlanes}(\mathbf{X_{new}}(\mathbf{r}, d_{new}))$;
  end
  Add design(s) found by EA to sampling plan;
  Simulate the new designs in the sampling plan;
  Interpolate $\mathbf{X}(\mathbf{r}, d)$ to common mesh;
end

4.2.3 Software

The CFD simulations were performed in the commercial flow solver Star-CCM+. All the surrogate modelling and design plan construction was performed in the Julia programming language [64] using the packages LatinHypercubeSampling.jl [65] for the sampling plans and ProperOrthogonalDecomposition.jl [50] for the POD construction. The RBF interpolation was done with ScatteredInterpolation.jl [66]

and the Differential Evolution algorithm was provided by BlackBoxOptim.jl [67]. The Nelder-Mead optimization algorithm was supplied by Optim.jl [68].

4.3 Test cases

4.3.1 Aerodynamic surrogate accuracy test

The surrogate model accuracy was tested on the generic vehicle model DrivAer [59], developed by the Technical University of Munich, in the estate configuration with a smooth underbody, closed rims and no cooling flow.

The method performance was investigated using three design parameters, for one dimension, roof angle; two dimensions, roof and diffuser height; and three dimensions, roof angle, diffuser height and front wheel deflector on/off, shown in Figure 4.7. The roof angle is varied from 0° to 22°, the diffuser height from

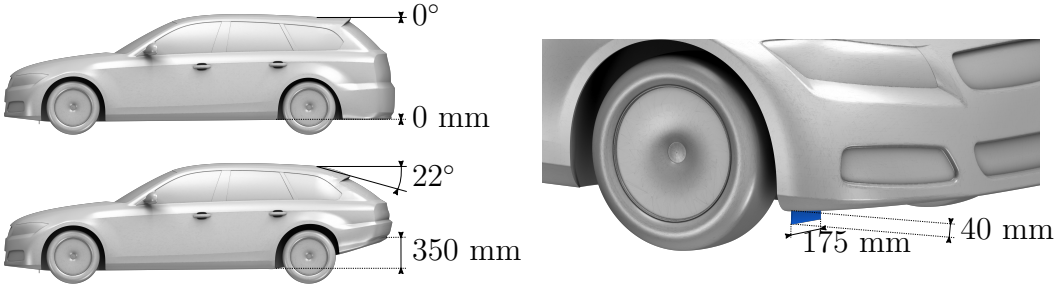

Figure 4.7: *Design parameters, roof angle, diffuser height and front wheel deflector.*

0-350 mm, with 0 mm being defined as a flat floor, and the front wheel deflector is either present or not. It should be noted that the investigated range for the design parameter is larger than what is typically considered when working with external vehicle aerodynamics.

Each simulation was run steady state for half the vehicle model using a symmetry plane boundary condition with a mesh consisting of approximately 22×10^6 hexahedral cells. The realizable $k - \varepsilon$ RANS turbulence model was used which, in combination with simulating half the model, reduces the computational costs by approximately an order of magnitude for each run compared the unsteady method used in Paper I. Ridge regression was not used for the aerodynamic accuracy comparison to retain an exactly interpolating surrogate model.

Wake force evaluation

Proper Orthogonal Decomposition requires the dataset to be ordered consistently between snapshots, which can be achieved through volume mesh deformation [57].

In this work, each CFD simulation was run on topologically different meshes. Each result when then interpolated to a common mesh without the vehicle body.

Since the flow field is interpolated to a mesh without a vehicle body, it was no longer possible to use the pressure and shear forces acting on the vehicle surface to compute the drag and lift. This was solved by evaluating $C_D A$ in the far field as

$$C_{\mathrm{D}} A = \int_S -C_{\mathrm{P}} - 2\left(\frac{V_{\mathrm{x}}^2}{V_\infty^2} - \frac{V_{\mathrm{x}}}{V_\infty}\right) \mathrm{d}S \tag{4.11}$$

where the integration planes, S, O, R and G, are defined in Figure 4.8.

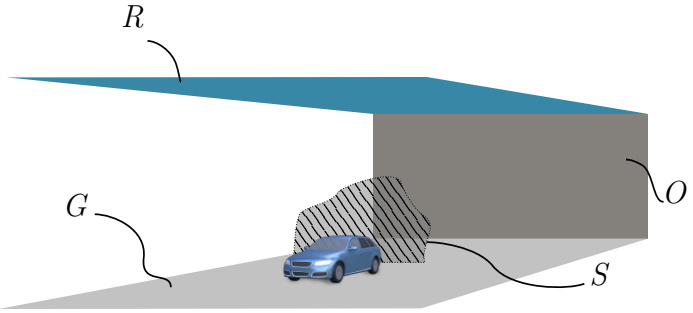

Figure 4.8: *Planes used to evaluate lift and drag. Wake plane S extends to the domain edges. O, R and G are the domains outlet, roof and ground respectively.*

4.3.2 Benchmark test cases

The surrogate model performance, when used for optimisation, was tested with nine benchmark functions. Each benchmark was started from five sample points in an optimised LHC sampling plan and run for 75 iterations where the surrogate model was recreated between each iteration.

When performing aerodynamic vehicle optimisation in a wind tunnel or using numerical simulations, the results from each test contain some level of noise. The repeatability when performing wind tunnel tests, without removing the vehicle, is on the order of $\pm 0.001\,\mathrm{C_D}$ [69] and typical changes to the vehicle drag vary from $0.005\text{-}0.050\,\mathrm{C_D}$ depending on the development stage. The optimisation method was benchmarked with 10 % noise to cover noise levels seen in aerodynamic vehicle optimisation. The ridge regression coefficient λ was treated as a hyperparameter for both the noise-free and noisy test cases as to not make any underlying assumption of the noise level to verify the methods ability to handle input data with varying levels of noise.

The nine benchmark problems used to evaluate the performance are included in Table 4.1, where a mix of multimodal, unimodal and multidimensional benchmark problems was used. The search space each function is tested on is presented in Table A.1, in the Appendix, as well as the coefficients for Hartmann function in

Table A.2.

Problem	Definition
f_1 Styblinski-Tang 2D	$\frac{1}{2}\sum_{i=2}^{2}(x_i^4 - 16x_i^2 + 5x_i)$
f_2 Rastrigin 2D	$20 + \sum_{i=1}^{2}[x_i^2 - 10\cos(2\pi x_i)]$
f_3 Rosenbrock 2D	$\sum_{i=1}^{2}[100(x_{i+1} - x_i^2)^2 + (x_i - 1)^2$
f_4 Beale 2D	$(1.5 - x_1 + x_1x_2)^2 + (2.25 - x_1 + x_1x_2^2)^2 + + (2.625 - x_1 + x_1x_2^3)^2$
f_5 Sphere 2D	$\sum_{i=1}^{2} x_i^2$
f_6 Perm d, β 2D	$\sum_{i=1}^{2}\left(\sum_{j=1}^{2}(j^i + \beta)\left(\left(\frac{x_j}{j}\right)^i - 1\right)\right)^2$
f_7 Goldstein-Price 2D	$[1 + (x_1 + x_2 + 1)^2(1914x_1 + + 3x_1^2 14x_2 + 6x_1x_2 + 3x_2^2)] * * [30 + (2x_1 3x_2)^2(1832x_1 + 12x_1^2 + + 4x_2 36x_1x_2 + 27x_2^2)]$
f_8 Hartmann 6D	$-\sum_{i=1}^{4}\alpha_i \exp\left(-\sum_{i=1}^{6} A_{ij}(x_j - P_{ij})^2\right)$
f_9 Rosenbrock 12D	$\sum_{i=1}^{1} 2[100(x_{i+1} - x_i^2)^2 + (x_i - 1)^2$

Table 4.1: *Benchmark test functions.*

The function output for each benchmark problem was scaled from 0 to 1 to facilitate comparison between each function. The results of each benchmark problem are presented in comparison with three other gradient-free optimisation algorithms, Random Search (RS), Differential Evolution (DE) and Nelder-Mead (NM). The surrogate model parameters used was 25 000 RBF hyperparameter iterations and 100 000 LHC sampling plan iterations. Each benchmark function is run a minimum of 100 times to gather statistics.

4.4 Results and discussion

4.4.1 Aerodynamic surrogate accuracy test

The accuracy of the interpolants is investigated in four cases, listed in Table 4.2. The constrained RBF and width refers to the use of the same RBF and width factor for all points, while for the variable RBF and width, it is optimised per

RBF centre, which in this case is per sample point. Note that the interpolant is optimised in each case. For cases A and B the engineering quantity, such as

Case	RBF, $\xi_{\text{RBF } i}$ & Width, ε_i	Scaling c_j
A	Constrained	None
B	Variable	None
C	Constrained	Adaptive
D	Variable	Adaptive

Table 4.2: *Surrogate performance configurations.*

measured distance or angle, is used directly as input to the surrogate while for cases C and D the engineering quantity is adaptively scaled. This is done for both the POD-based and force-based surrogate model.

Each dimension investigation is performed by running a design of experiments of 101 CFD simulations, where a subset of the simulations are used to create the surrogate model and the remaining points are used as a validation set. The surrogate model performance indicator used is the Mean Absolute Error (MAE)

$$MAE = \frac{\sum_{i=1}^{n} |f_i - \tilde{f}_i|}{n} \tag{4.12}$$

where f_i is the i-th CFD result, or ground truth, and $\tilde{f}_i$ is the i-th surrogate prediction. In the case of the two- and three-dimensional test cases, the sample points are chosen as a subset of a LHC plan containing all 101 simulations, with the subsets being 10, 20 and 40 sample points. The subset is chosen by optimising the Audze-Eglais error as a subset from the original plan to reduce the computational cost of running a new simulation to investigate the influence of sample number on the performance.

Due to the method being stochastic, each interpolant is created 25 times. The presented performance data indicates the median performance with ±95% confidence interval for the median unless stated otherwise. The samples from which the median is created are also shown; however, for illustration purposes the y-axis is limited and some outliers might not visible.

The roof angle is used to investigate the surrogate model performance for one dimension. In one dimension no relative scaling is used, i.e. it is only cases A and B which are investigated, Figure 4.9.

Both surrogate models perform similarly for 20 and 40 samples while the POD-method performs worse for 10 sample points. The spread between samples is larger for the POD-based surrogate, particularly for case B with 10 sample points. This is likely due to degrees of freedom being too large for the number of sample points, leading to overfitting. For two dimensions, roof angle and diffuser height, the results are similar to the one-dimensional test. However, the inclusion of another

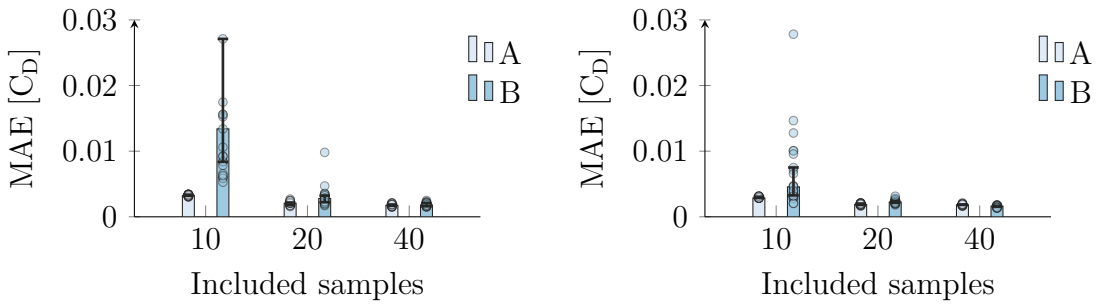

(a) *POD-based surrogate performance.* **(b)** *Force-based surrogate performance.*

Figure 4.9: *1D, surrogate performance. Bar of the median performance, error bars indicate the ±95% confidence interval for the median. The samples are shown as circles.*

design dimension reduces the surrogate models predictive capability, especially for cases A and B which can be seen in Figure 4.10.

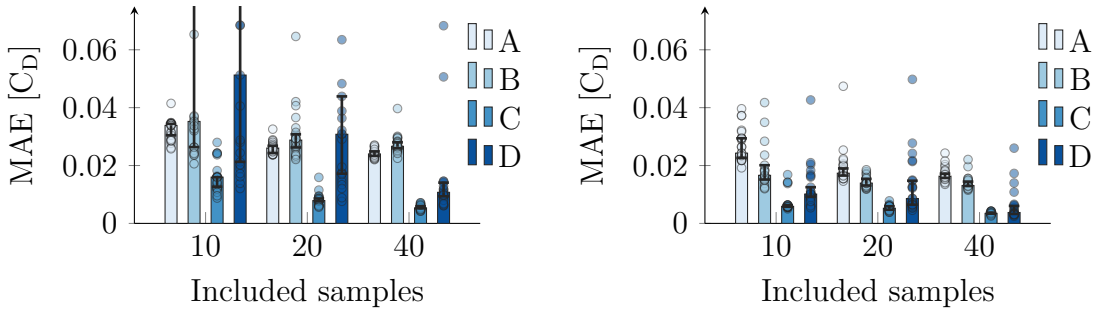

(a) *POD-based surrogate performance.* **(b)** *Force-based surrogate performance.*

Figure 4.10: *1D, surrogate performance. Bar of the median performance, error bars indicate the ±95% confidence interval for the median. The samples are shown as circles.*

The inclusion of adaptive axis scaling reduces the error when the number of samples increase. Even though the confidence interval of the median is large, the force-based surrogate model consistently outperformed the POD-based surrogate in predictive accuracy. The trends for the three-dimensional case are similar and are not shown here.

4.4.2 Prediction error

The prediction error for each sample is investigated further for the one dimensional case, Figure 4.11b. The performance is largely within $0.005\,C_D$ absolute error except around 16° roof angle, where the error increases. Figure 4.11a shows all 101 CFD simulations as well as the sample locations for the 10 samples. At around

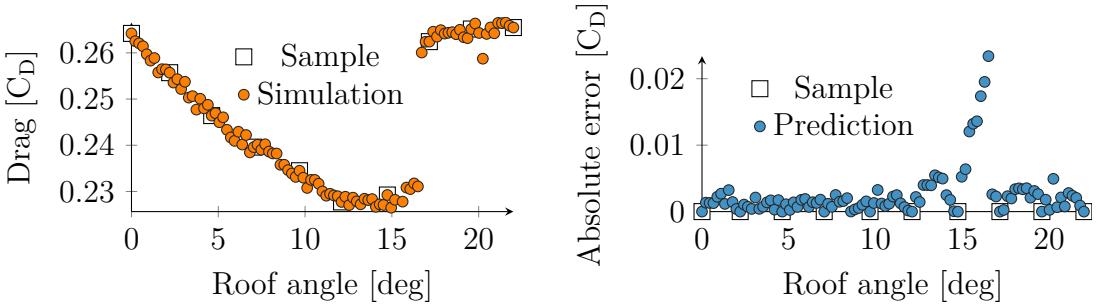

(a) *Simulated drag values of all 101 simulations for varying roof angle.*

(b) *Performance of the median force-based surrogate for 10 sample points, case C.*

Figure 4.11: *Performance of the median force-based surrogate for 10 sample points, case C.*

16° the simulation results are discontinuous. This is due to the flow separating from the roof causing a sudden increase in drag. It is believed that the limited increase in surrogate performance, as the number of samples increase, is due to the discontinuity in drag. Moreover, it is a known fact that the performance of RBF interpolation suffers in the neighbourhood of discontinuity or strong gradients [70, 71].

The POD-based method's relatively poor performance at 10 sample points is investigated further using the mode convergence method presented in section 3.2.3. The mode $\phi_{i,end}$ is the i-th mode used for comparison, containing the snapshots for all 101 designs. The snapshot convergence for the first 10 modes are presented in Figure 4.12. The first POD mode indicates convergence; however, the remaining 9

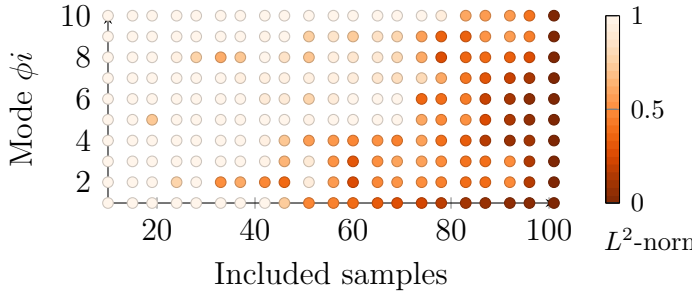

Figure 4.12: *Convergence history of first 10 POD modes.*

modes do not. The energy contained in each mode gives an idea of the number of modes needed to capture the variance in the dataset. Figure 4.13 shows the energy contained in each POD mode based on all 101 simulations. The first mode contains a large portion of the overall energy (83 %); however, 77 modes are needed until 99 % of the energy is captured. Since a large number of snapshots are needed, it indicates that there is not much underlying generality in the dataset which can be extracted using POD for this problem. It is a known fact that POD is not capable

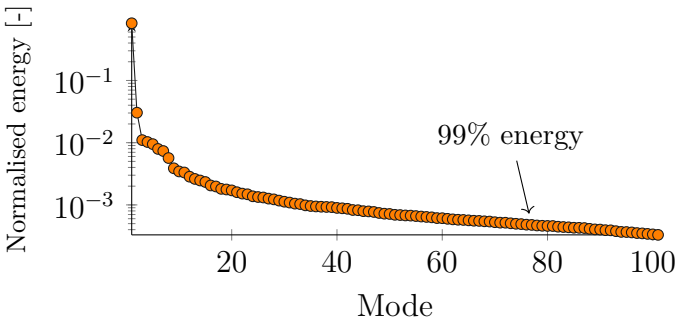

Figure 4.13: *Normalised energy per POD mode.*

of decomposing travelling wave problems which might explain the slow convergence and the large number of POD modes needed to reconstruct the dataset [48].

Categorical LHC performance

The third design parameter is the front wheel deflector on/off. In this thesis the Latin Hypercube Sampling plan was extended to include categorical, or discrete, design parameters. The performance difference between using separate LHC plans per category or using one categorical LHC is presented here. In this comparison, a subset of 20 sample points is used. Out of these 20 points, 10 are used to create a surrogate for the front wheel deflector on, while the other half is used to create a surrogate for the front wheel deflector off. These two separate surrogates are compared with a surrogate model using all 20 points. This process is repeated 25 times for cases A and C to gather statistics due to the stochastic nature of the surrogate creation.

The results can be seen in Figure 4.14 where the performance for the unscaled surrogate model, case A, indicates a small benefit of using the categorical LHC plan. The performance when using adaptive scaling improves for the separate LHC plans

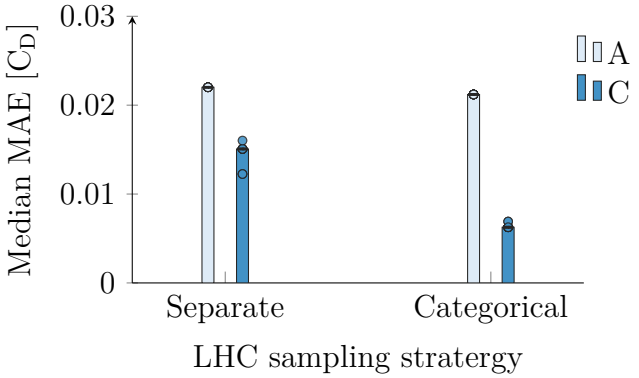

Figure 4.14: *Separate LHC plans compared with one categorical plan for cases A and C using 20 sample points in total.*

as seen previously; however, when building the surrogate from the categorical LHC plan the overall predictive capability of the surrogate model is greatly improved. Note that the error bars for the median are small and not visible in Figure 4.14. The negligible performance gain for case A when using the categorical LHC is thought to be limited by the compromise of choosing RBF and width factor when the included design parameters are of largely differing scales. This is similar to the interpolation performance comparison of the three camel hump function presented in section 4.2.2.

4.4.3 Benchmark test cases

Based on the accuracy of the aerodynamic test cases, the adaptively scaling surrogate models, C and D, are selected for further benchmarking with test functions f_3 and f_8, in Figure 4.15.

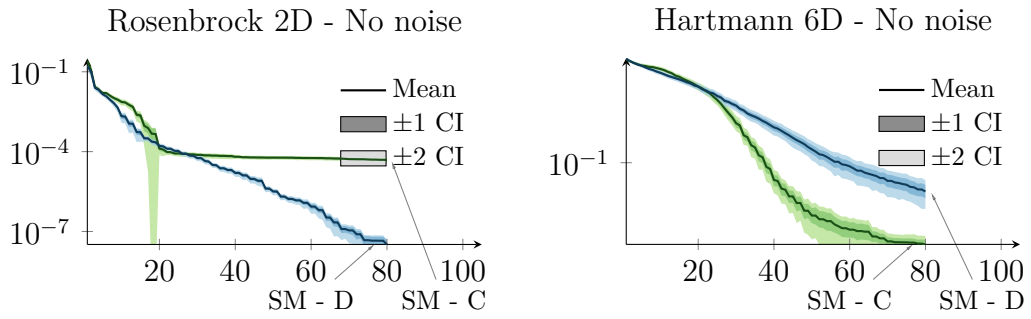

(a) *Rosenbrock 2D benchmark function.* **(b)** *Hartmann 6D benchmark function.*

Figure 4.15: *Surrogate model optimisation performance on two test functions using surrogate model versions C and D.*

The increased flexibility of surrogate model D in the two-dimensional case increases the convergence speed after approximately 20 function evaluations. The six-dimensional test function indicates slower convergence when using surrogate model D, which is thought to be due to overfitting when the number of samples is small compared to the number of dimensions. Since it is not clear at which point there are enough samples to use surrogate model D, the benchmark results were performed for surrogate model D.

Two of the results are shown in Figure 4.16 which are representative of problems seen in aerodynamic optimisation, namely high dimensional functions and multimodal functions. The NM algorithm, which has good performance for some of the noise-free benchmark problems, tends to converge prematurely due to the added noise and performs worse than the RS algorithm for all of the noisy benchmark problems. The convergence history for all nine benchmark functions without and with noise, can be found in the Appendix, Figure A.2 and Figure A.3, respectively.

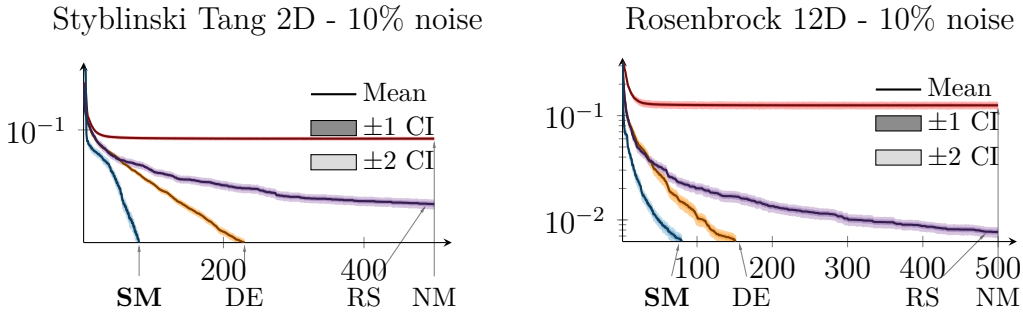

Figure 4.16: *Optimisation benchmark performance, functions f_1 and f_9 with 10% white noise. Results are normalized by the test function maximum and minimum value.*

The surrogate model shows good initial convergence speed which is important when optimising with a fixed time budget. The surrogate model performed better than or as good as the other algorithms, on 16 out of the 18 investigated benchmark problems. It required half the functions calls on averaged compared to the second best algorithm for the noisy test functions. The results indicate that the SM optimisation algorithm is robust and high performing. It is also capable of handling a low number of initial samples and works with functions containing noise.

Chapter 5

Optimisation and wake aerodynamics

The previously presented optimisation method was developed to facilitate the creation of low-drag reference geometry and subsequent study of the resulting flow field. This chapter contains preliminary results of, at the time of writing, unpublished work and is part of a collaboration between Chalmers University of Technology and Loughborough University.

5.1 Background

In a study by Howell et al. [72], it was stated that two cars with the same zero yaw drag could have significantly differing cycle averaged drag. This highlights the possible benefits of considering the cycle-averaged drag during vehicle development.

Two recent studies, investigating the influence of asymmetric rear tapers at yaw, found that the yaw-performance improved by increasing windward taper angle, and reducing the leeward taper angle compared to the optimal 0°-yaw condition, [17, 73]. In the study by Varney et al. [17], the rear end was tapered, keeping the length of the vehicle constant, while Garcia de la Cruz et al. [73] used rearward facing flaps to achieve a similar effect. Garcia de la Cruz et al. [73] found that, as the length of the flaps increased, the drag reduction increased significantly using asymmetric flap angles, whereas symmetric flaps were not significantly influenced by the flap length.

Howell [9] showed that the drag increase at yaw is related to the lift and side force of the vehicle. Depending on the vehicle shape the drag increase at yaw either increased or reduced with increasing lift. The complete picture of the wake flow field, in relation to the drag increase at yaw, is still not fully understood. Based on the results from the previously presented work on yawed flow, as well as the available literature, it is theorised that there is potential for further drag reduction by manipulating the wake balance using a combination of an asymmetric roof- and side-tapering which is investigated here using the previously presented optimisation method.

The strength of optimisation algorithms is the ability to find good performing solutions in vast design spaces with few function evaluations. This ability is influenced by the quality of the numerical- or experimental-setup and is also affected by the objective function. The optimisation algorithms ability to find

good-performing solutions can lead to the exploitation of weaknesses in the setup procedure rather than improving the design. [74] This highlights the importance to reason about and study the resulting solution to increase the understanding of what caused the performance change.

5.2 Methodology

The potential for drag reduction using asymmetric roof- and side-tapering was investigated numerically and experimentally using the generic Windsor body by: first, optimising a rearward facing cavity using numerical simulations; second, optimising nine separate kick geometries in experiments.

5.2.1 Geometry

The generic Windsor body is 1044 mm long making it approximately ¼-scale, and has been used in several studies, for example [17, 23, 72]. The variant with wheels was used, together with a 50 mm deep cavity, Figure 5.1. The model is held in

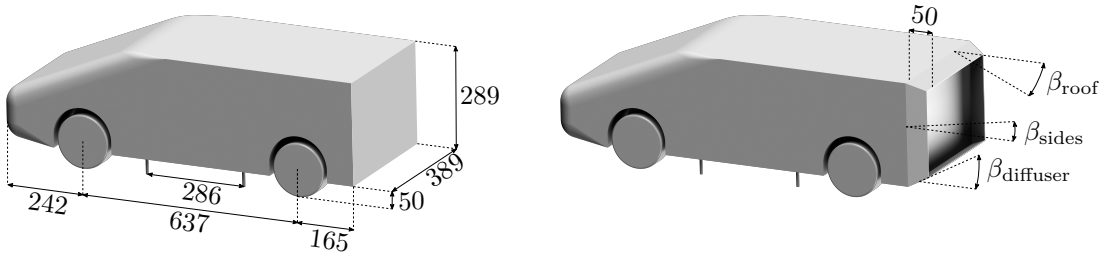

(a) *Baseline geometry.* **(b)** *Cavity tapering.*

Figure 5.1: *Windsor model with wheels. Measurements are given in* mm

place with four 8 mm threaded bars. The wheels are 55 mm wide with a diameter of 150 mm and are not rotating. Underneath each wheel there is a 3-4 mm deep machined groove in the floor.

The kick geometry covers the sides and the roof of the geometry. Each side is split into three sections resulting in a total of nine kicks, numbered from 1-9 in a clockwise fashion facing the rear of the vehicle, Figure 5.2a. The limited number of kick angles per side is expected to influence the maximum achievable drag reduction. In the tests the model was yawed nose left due to the location of the imaging equipment in the tunnel. However, to bring it in line with the convention of SAE standard J1594 [75], the results are reflected along the symmetry line as if the model was yawed nose right. I.e. the wind appears as if it is coming from left to right in the vehicle driving direction in the presented figures and results. This is consistent with the direction of the previously presented yawed flow in this thesis.

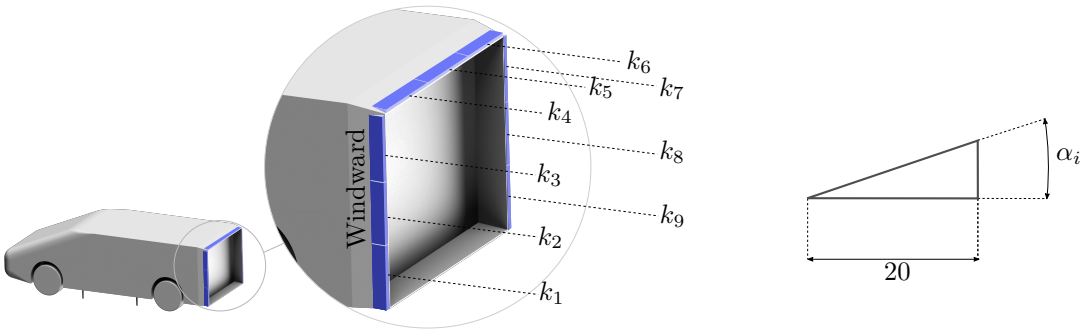

(a) *Naming convention for individual kicks.* **(b)** *Kick geometry.*

Figure 5.2: *Kick geometries on the cavity. Measurements are given in* mm.

A side view of the kick geometry can be seen in Figure 5.2b where the angle α_i denotes the kick angle of the i-th kick. The setup was limited to positive kick angles only and does result in sharp edges between adjacent kicks when different kick angles are used. This is expected to reduce the maximum achievable drag reduction. The kick geometries were 3D printed, with locating pins for mounting, in four angles, 0°, 7°, 14° and 21°. The width of each kick is 20 mm, or 2 % of the vehicle length. Each segment kick length is 120 mm on the roof and 90 mm on the sides.

5.2.2 Optimisation

Cavity angles

First the cavity angles for the sides, roof and diffuser were optimised using the previously presented force-based surrogate model where an ensemble of adaptively scaled Radial Basis Function interpolants was used. The surrogate model was started from a LHC sampling plan containing 15 samples, where the angles were allowed to vary from 1-25°.

The side angle was constrained to be the same left to right. The objective function used for the optimisation was the cycle averaged drag, C_{DWC}, variant used by Varney et al. [17],

$$C_{\mathrm{DWC}} = 0.53C_{\mathrm{D0}} + 0.345C_{\mathrm{D5}} + 0.13C_{\mathrm{D10}} \tag{5.1}$$

meaning that each function evaluation required three simulations. The optimisation was run in an alternating fashion between the lowest cycle averaged drag and the largest standard deviation in the ensemble.

Kick angles

The kick angles were optimised in the Loughborough Large Wind Tunnel using the same surrogate model but constrained to the four angles, 0°, 7°, 14° and 21°. The surrogate model was started from five samples, four from an optimised categorical LHC sampling plan, as well as the case where the cavity is smooth, i.e. all kick angles are set to 0°. Since the number of possible design is finite, $4^9 = 262144$, each location was sampled in the surrogate model to find the lowest drag value and highest standard deviation in the ensemble each iteration. Both the lowest drag value and the highest standard deviation was tested before running the surrogate model again with the information from the two new designs added to the model.

The optimisation was run separately for 0°-, 5°- and 10°-yaw, with the objective function being minimum drag. The idea was to simulate the ability of the geometry to adapt to the surrounding wind conditions. At 0°-yaw a symmetry constraint was imposed, i.e. $k_1 = k_9$, $k_2 = k_8$, $k_3 = k_7$, $k_4 = k_6$. The sensing of the side wind direction and related implementation details were not part of this work.

To investigate the potential of sectioning the geometry, the optimisation was first run with the constraint that each side needed to use the same angle, reducing the number of design parameters from nine to three. Once finished, the information from the constrained design space was added to the full design space surrogate model, together with four additional LHC sampling points in order to add information from the full design space.

To test all possible design combinations a total of $4^5 + 4^9 + 4^9 = 525312$ tests would be needed. As this is not feasible in a given time frame, guaranteeing that the optimum has been found is not possible. However, it is expected that the function is smooth locally. Based on this reasoning, and a finite amount of time available for testing, the optimisation routine was stopped when it was deemed that there no longer was a design, in the vicinity of the already tested designs, that would improve the objective function further.

5.2.3 Numerical set-up

The roof, sides and diffuser angles were optimised numerically using a RANS, k-ω SST turbulence model. A steady state model was chosen due to the reduced computational cost compared to an unsteady method. Optimising the extensions to reduce the cycle averaged drag is especially expensive considering that each function evaluation requires the simulation to be run at three different yaw angles. The computational domain is made to resemble the physical wind tunnel, which will be presented in the next section, to model the influence of the boundary layer growth, as well as the blockage. The inlet velocity was tuned to achieve a test section velocity of 40 m/s, resulting in a Reynolds number of $Re_{\mathrm{H}} = 7.38 \times 10^5$ based on the vehicle height. The simulations featured stationary wheels as well as

the gap underneath each wheel to match the wind tunnel conditions.

Mesh

Figure 5.3 shows a mesh study of the baseline geometry from 15×10^6 to 150×10^6 cells, where the predicted drag increase at 10°-yaw is shown. The drag increase is

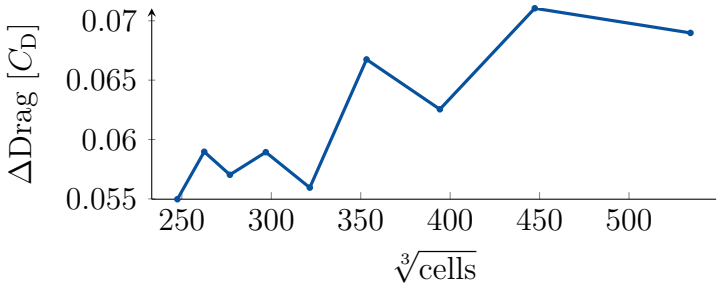

Figure 5.3: *Mesh study of the baseline geometry where ΔC_D is the difference in drag between 0°- and 10°-yaw.*

plotted against the cube root of the number of cells, as this is related to the edge length of each cell in a hexahedral mesh, which in turn, is related to the spatial discretisation accuracy. Plotting the drag change against the cell count can give a false impression of mesh convergence due to the rapidly increasing cell count as the cells edge length decreases. The increasing drag difference, as the number of cells increase, is mainly related to the drag prediction at yaw changing as the cell count is increased. It is believed that the lack of mesh convergence is due to the problem being inherently unsteady and the results tending more towards an unsteady solution as the grid is refined.

To balance the computational cost and the number of affordable optimisation iterations, the mesh containing approximately 90×10^6 hexahedral dominant cells was used employing a low $y^+ < 1$ modelling approach, similar to the previously presented work. An open question that remains, is how the cell count influences the predicted optimum location in the design space.

Unsteady simulations

Unsteady simulations using IDDES of the baseline geometry and the optimised cavity were also made in order to study the resulting flow field with higher fidelity before the tunnel measurements were made.

The setup follows the previously presented method; however, the timestep was reduced to $2.0 \times 10^{-4}s$, due to the increased testing velocity. The averaging time was also reduced to 2 s due to the reduced scale and increased velocity. Figure 5.4 shows the two simulation methods as well as the wind tunnel results of the baseline geometry. The prediction in terms of absolutes improves when

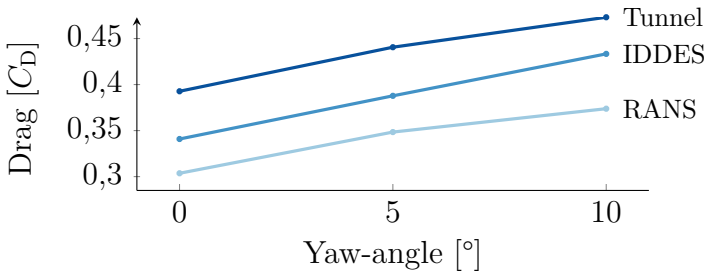

Figure 5.4: *RANS, IDDES and wind tunnel test results of the baseline geometry.*

switching to an unsteady method, which is expected due to the large separated wake of the baseline geometry. The predicted trend is similar for both methods with RANS underpredicting the drag at 10°-yaw. The absolute prediction error is larger than what is expected compared to full-scale testing; however, there are several possible geometric factors which can influence the results, especially at model scale, such as leakages, gaps in the model, surface roughness and mounting hardware, all of which were not modelled in the simulations.

5.2.4 Physical testing

The wind tunnel tests were performed in the Loughborough Large Wind Tunnel which is an open return, closed test section facility. The cross-sectional area of the test section is 2.5 m resulting in a blockage ratio of 4.7 %. With an empty test section, the flow uniformity is ±0.4 % with a turbulence intensity of 0.2 % [76].

Base pressures and forces were collected for 300 s for each tested configuration. The repeatability of the tests was investigated by gathering balance measurements each testing day of the cavity with 0° kick angle for all kicks, resulting in 7 samples. The estimated uncertainty, for a 95 % confidence interval, is ±2 counts at yaw and ±1 count at 0°-yaw. The model was not removed from the balance during the entire time period covering the kick angle optimisation.

5.3 Results and discussion

The results for the numerical optimisation of the cavity angle will be presented first, followed by the experimental optimisation study of the separate kick angles.

5.3.1 Cavity optimisation

The cavity geometry was optimised over a total of 42 simulations. Each design iteration, as well as the best current solution, is shown in Figure 5.5 where the first 15 iterations are part of the sampling plan. A predicted improvement of 51 counts

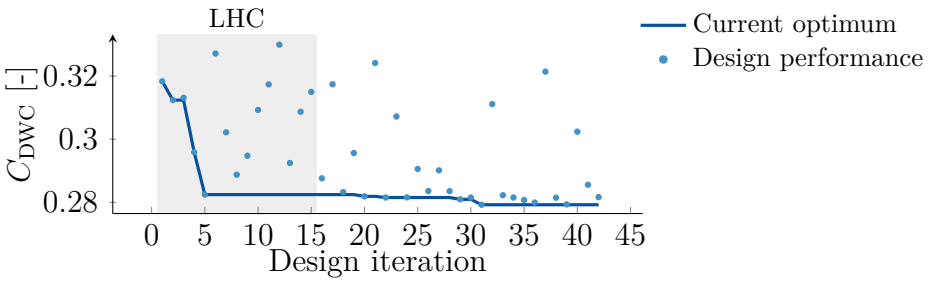

Figure 5.5: *Cavity optimisation history.*

C_{DWC}, over the baseline geometry without a cavity, was found.

The predicted optimum has a roof angle of 12.6°, diffuser angle of 1° and side tapering of 13.5°. Designs with lower 0°-yaw drag were found; however, some designs with low drag at 0°-yaw were found to have larger increases in cycle averaged drag. For example, a design featuring a roof angle of 7.1°, diffuser angle of 25° and side tapering of 10.7° was found to have identical 0°-yaw drag to the optimum but a 5 % larger cycle averaged drag, highlighting the importance of considering representative operating conditions.

Howell [9] noted a linear relationship between the drag increase at yaw and the lift of the vehicle at yaw. A similar relationship was seen in the results here; in addition, similar trends in all the force and moment coefficients could be observed. Figure 5.6 shows the cycle average drag as a function of the lift at 10°-yaw, where a trend between increasing lift and reduced cycle average drag can be seen. While

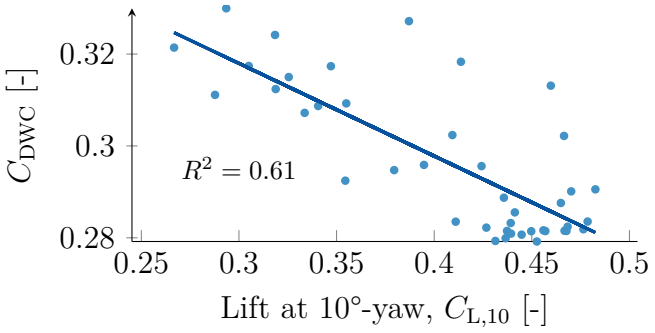

Figure 5.6: *Cycle averaged drag in relation to lift for all configurations in the taper angle optimisation.*

there is a trend, the spread is large, and lift alone is not a good indicator of the vehicle performance in this study. Howell [9] also noted that the vehicle shape influences the slope of the trend, even switching sign depending on if the vehicle is of a 2-box or 3-box type shape.

Design sensitivity

The sensitivity to changes in the side taper and roof angle was investigated by keeping the diffuser angle constant at 1° and using the surrogate model to predict the cycle-averaged drag throughout the remaining design space. The design area from approximately 10° to 15° in both side tapering and roof tapering angle are within 3 counts of the optimum location, Figure 5.7. Each simulated design with a

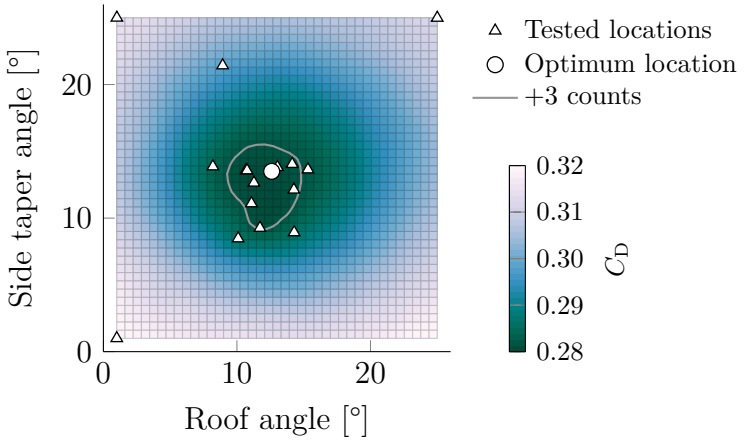

Figure 5.7: *Sensitivity to roof- and side taper-angle for a fixed diffuser angle of* 1°. *Tested design locations include all designs with a diffuser angle below* 2°.

diffuser angle of less than 2° is also shown in the figure to indicate the surrogate model coverage in the vicinity of the optimum. According to the predictions acquired from the RANS simulations, the sensitivity is low in the vicinity of the optimum.

Due to the low sensitivity in the region near the optimum, a design with more taper angle compared to the optimum was chosen to increase the available space for the kick geometry. The design that was manufactured features a 14° side- and roof-tapering. Since the optimisation pushed the diffuser angle to the lowest allowed setting, it is likely that better designs exist outside the covered design space, but this was not investigated in this work. To ease manufacturing the diffuser was set to 0°.

Manufactured design

The manufactured design was investigated further numerically using the presented unsteady simulation method. As the model is yawed, the wake becomes increasingly upwash dominated along the centerline, Figure 5.8. At 0°-yaw the wake is downwash dominated and not in-line with what typically depicts a balanced wake where the velocity vectors are perpendicular to the base. Perry [32] investigated the top and bottom tapering using the same geometry without wheels and found that a 16° top

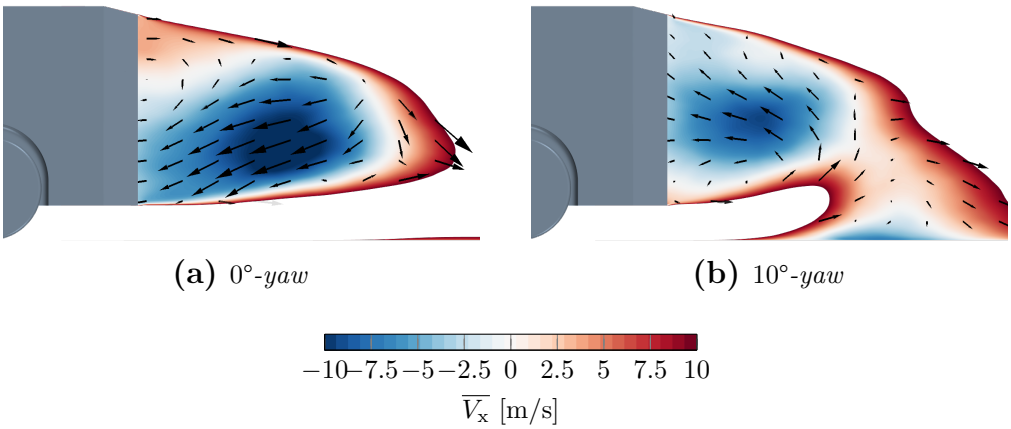

(a) 0°-*yaw* **(b)** 10°-*yaw*

Figure 5.8: *Mean longitudinal velocity, body axis centerline view.*

taper with a 6° bottom taper produced the lowest drag and a balanced wake. The wake seen for this geometry at 0°-yaw is not an expected optimum for 0°-yaw drag; however, since the optimisation objective is the cycle-averaged drag, a trade-off in performance between the three yaw angles is made when improving the design.

It is believed that the trend between lift and cycle-averaged drag is the result of the wake balance shifting when lift is changed. With this reasoning, it is expected that the cycle-averaged drag would begin to increase with increasing lift at some point, as the drag increase at 0°-yaw is outweighed by the reduction in drag at yaw. There are indications of the cycle-averaged drag hitting a plateau with increasing lift in Figure 5.6, however further analysis covering more of the high lift designs is needed to confirm this observation.

As mentioned, the manufactured cavity is 50 mm deep, featuring a 14° side- and roof-tapering with a flat floor. The predicted reduction in cycle averaged drag for the RANS and IDDES simulations for this geometry are 14.7 % and 15.3 % respectively. The reduction in C_{DWC} when adding the cavity measured in the wind tunnel was 19.2 ± 0.3 %.

5.3.2 Kick angle optimisation

The kick angle is optimised separately for each yaw angle without trading any information between them. This is done in order to see whether the optimum is found in the same region of the design space for both 5°- and 10°-yaw without using the knowledge available at the other yaw angle. A more efficient approach would be to include the yaw angle as a design parameter, allowing information to be traded between each yaw angle.

The kick angles are first optimised to use the same angle per side to reduce the design space, after which the full design space is used including the information in the constrained space. Each yaw angle is started from a LHC sampling plan

including 4 design points as well as the configuration with 0° kick angle all around. The configuration with 0° kick angle all around, i.e. a smooth taper is referred to as the smooth cavity here. For the yawed cases an additional LHC plan of 4 points was added after the constrained design space optimisation was finished, to add non-uniform information.

A total of 111 designs were tested in the wind tunnel, 26 at 0°-, 39 at 5°- and 46 at 10°-yaw. The optimisation history of the 0°-yaw condition can be seen in Figure 5.9 where the fifth design is the smooth cavity. At 0°-yaw an improvement

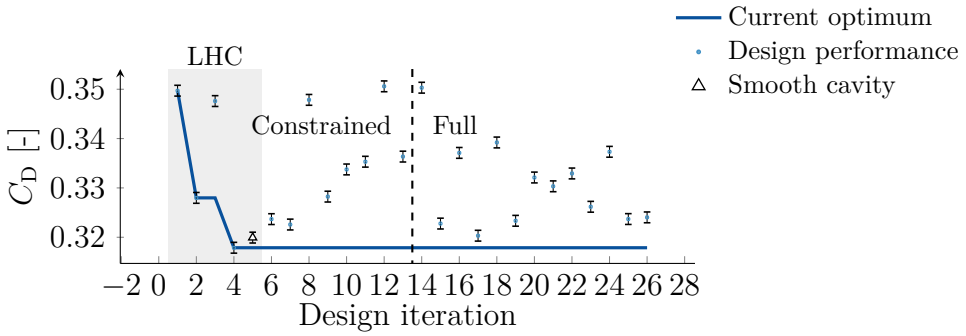

Figure 5.9: *Kick optimisation history at* 0°*-yaw. Error bars indicate the* 95 % *confidence interval.*

of 2 drag counts was found using a 7° kick angle across the roof. While small, the improvement is outside the margin of error and is expected due to the downwash dominated wake of the smooth cavity. None of the designs in the constrained space were found to improve the 0°-yaw drag further.

Figure 5.10 contains the optimisation history of the yawed case. For both yaw angles, an improvement over the smooth cavity, outside the confidence interval, was not found in the constrained space. Base on the work from Varney et al. [17] and Garcia de la Cruz et al. [73] on asymmetric tapering and yawed flow, it was expected that adding the kick to the leeward side in either a 7° or 14° taper angle would improve the drag at yaw; however, for both yaw angles, these configurations were within the reported confidence intervals.

It was only possible to improve the design over the smooth cavity with significance using the full design space. For both yaw angles the optimum design featured the kick angles 0°,0°,0°,0°,0°,7°,0°,7°,14°, shown in Figure 5.11. Each design with a significant drag reduction featured changes toward the leeward side of the model, kick positions 6-9 (counting clockwise).

The sensitivity to kick angle changes was investigated by keeping all angles constant at the optimum and changing one at the time. Configurations that were not tested in the tunnel are estimated using the surrogate model. In Figure 5.12 the sensitivity at 5°-yaw is shown, the sensitivity map for 10°-yaw showed similar trends. It should be noted that it is only the explicitly tested configurations which

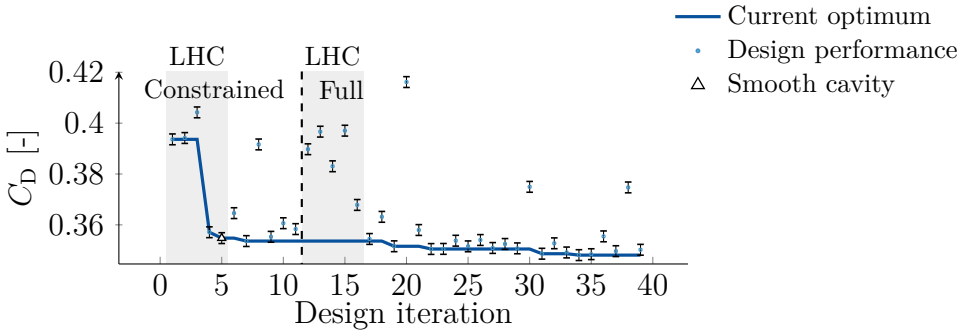

(a) 5°-*yaw.*

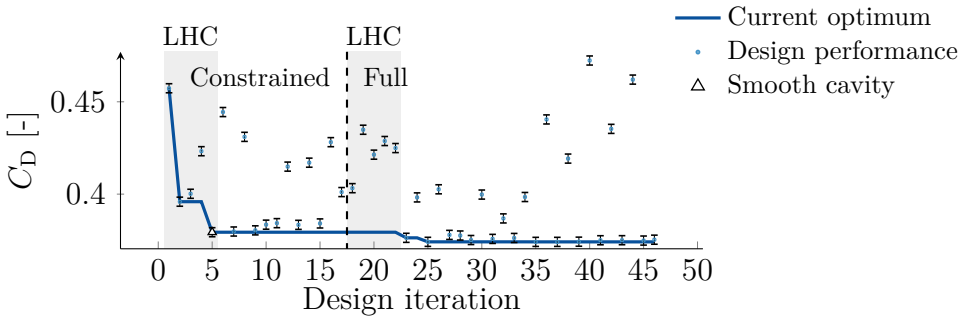

(b) 10°-*yaw.*

Figure 5.10: *Kick optimisation history at yaw. Error bars indicate the* 95 % *confidence interval.*

are marked in Figure 5.12. There are several designs in close proximity to the optimum in the design space but these designs featured more than one change and are not shown. Strong gradients in the drag sensitivity toward the windward side of the model can be seen, kicks 1-4. This strong gradient suggests that further drag reduction could be achieved by introducing negative kick angles, and is an expected result [17, 73]. However, for manufacturing and testing time purposes, the angles were limited to positive kick angles. Unexpectedly the leeward roof angle, kick 6, had an optimum which was non-zero. All configurations with a drag reduction of more than 4 drag counts at yaw featured a non zero kick angle in position 6, proving to be crucial in order to achieve larger drag reductions.

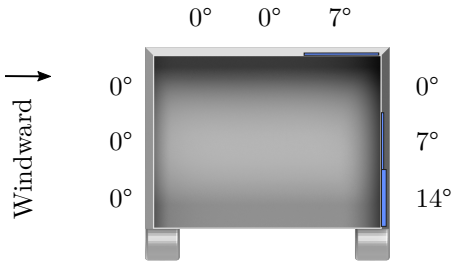

Figure 5.11: *Windsor model optimum kick angles.*

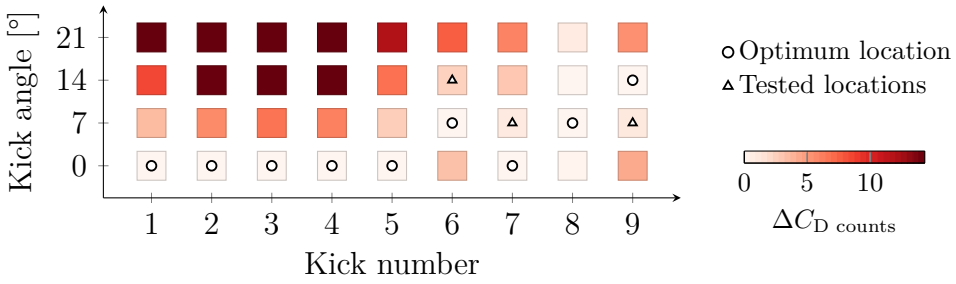

Figure 5.12: *Sensitivity to kick angle changes of each kick, while keeping the other kick angles constant at the optimum. Tested design locations only include designs which were explicitly tested.*

The base pressures at yaw, Figure 5.13, indicate a lateral symmetrisation of the wake when adding the optimised kicks. Overall the base pressure for the optimum

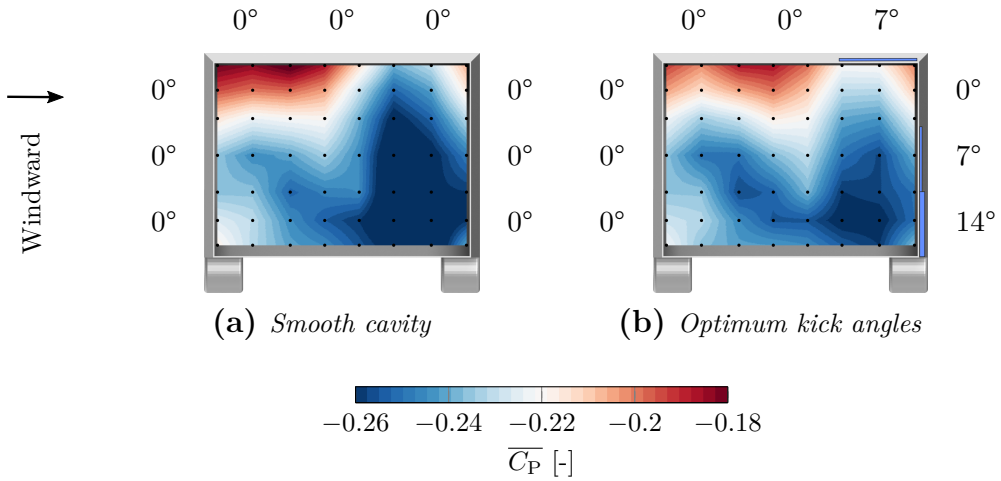

(a) *Smooth cavity* **(b)** *Optimum kick angles*

Figure 5.13: *Experimental base pressure at 5°-yaw of the smooth cavity and optimised kick angles. The samples points are marked in black.*

is more uniform using the kicks, with reductions in both the high and low pressure areas. The main contributor to the drag reduction at yaw is the increased base pressure inside the cavity, although a reduction in suction along the outer surface of the cavity near the non-zero kick angles is expected.

Since the leeward roof kick angle gave an unexpected reduction in drag, it was investigated further separately to isolate the influence on drag. The investigated configuration featured 0° kick angles on the windward side and 7° kick angles on the leeward side, Figure 5.14. The inclusion of the leeward roof angle reduced drag by 3 C_{D} counts and the majority of the base pressure increase is located around the leeward upper wake. The lateral base pressure change suggests that the base pressure improvement is due to a change in the lateral symmetry of the wake. However, this needs to be investigated further with wake measurements.

The standard deviation of the base pressure fluctuations, show in Figure 5.15,

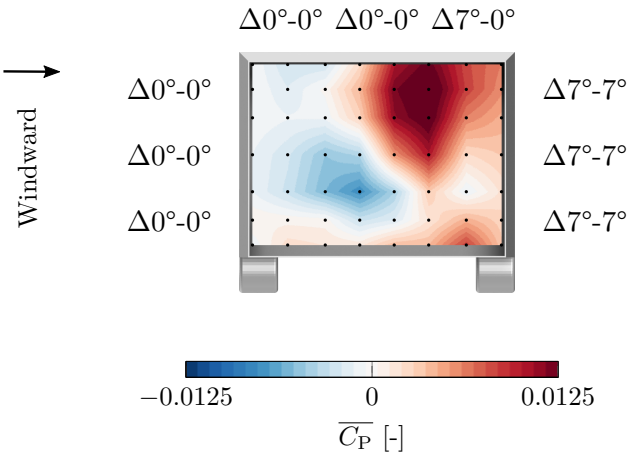

Figure 5.14: *Experimental base pressure delta at 5°-yaw where the change is the kick angle a position 6. $\overline{C_P}$(0°,0°,0°,0°,0°,7°,7°,7°,7°)-$\overline{C_P}$(0°,0°,0°,0°,0°,0°,7°,7°,7°) at 5°-yaw. The sampled points are marked in black.*

show an increase in the unsteadiness of the base pressure near the centre of the base. Increasing base pressure fluctuations have been linked with increases in drag [77]. Perry [32] found that by increasing the front radius of a simplified one-box model, the unsteadiness of the base pressures generally increased by reducing the shear layer thickness and increasing mixing in the wake. However, this did not

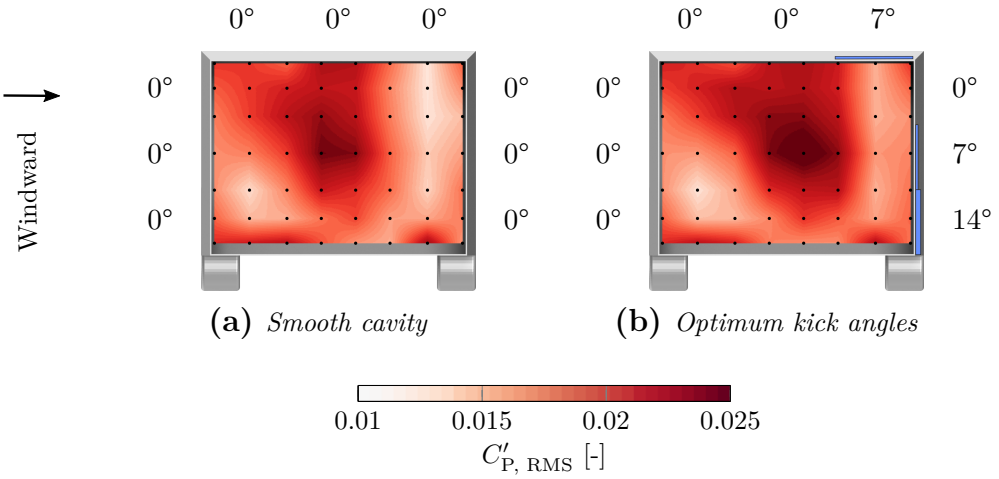

Figure 5.15: *Experimental base pressure at 5°-yaw of the smooth cavity and optimised kick angles. The samples points are marked in black.*

consistently increase base drag and was found to be influenced by the model ground clearance. Other authors have noted that the most stable wake is not always consistent with the lowest drag [30, 78]. The addition of the kick angles in this investigation likely increases the size of the wake and subsequently the mixing in the wake, consistent with the increase in base pressure fluctuations. Both the

overall drag and the base drag are reduced with the optimum kick angles over the smooth cavity. The reduction in base drag, in addition to the increased base pressure fluctuations, indicate that the optimised kick angles improve the drag by influencing the mean bulk flow. A question which arises from this work is whether unsteady high-frequency flow control of the kick angles, in an attempt to reduce the momentum mixing in the shear layers, could lead to further drag benefits. It is also of interest to study whether the addition of unsteady high-frequency flow influences the optimum kick angle positions.

At the time of writing this work, bulk flow measurement data was not available; however, unsteady simulation results of the smooth cavity were investigated. Figure 5.16 shows the body normal wake plane 100 mm behind the vehicle. The optimised kick angles are also shown in the figure to ease the discussion of the resulting optimum, note that the flow field is of the smooth cavity. A large

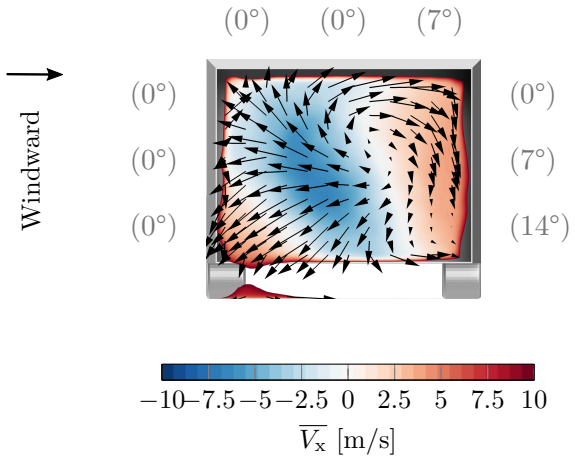

Figure 5.16: *Windsor model CFD simulation of smooth cavity. The wake plane is located* 50 mm *behind the vehicle coloured by longitudinal velocity. The optimum kick angles were not included in the simulation but are shown in gray in the figure for convenience.*

scale clockwise rotation is visible in the wake and the overall wake shape at yaw is qualitatively similar to the previously presented results of the fully detailed geometry from Paper I. It is believed that the bottom two leeward kick angles, 8 and 9 (7° and 14° respectively), are a result of the optimisation process improving the lateral symmetry in the wake. The optimum of the two kick angles closest to the top leeward corner, kicks 6 and 7 (7° and 0° respectively), were an unexpected result from the optimisation study. Based on the simulation results of the smooth extensions, it seems like the leeward roof kick, number 6, acts to prevent the downwash toward the leeward side while the 0° angle of kick 7 reduces the lateral velocity. The global effect of these kick angles, 6 and 7, is believed to reduce the overall clockwise rotation of the wake. As this is preliminary results, further analysis

needs to be performed using wake flow measurements to investigate changes in the bulk wake flow resulting from different kick angles.

As stated previously in this thesis, it is not a trivial task to single out causes of drag changes as the performance consists of non-linear trade-offs and complex three dimensional interactions. In this work, optimisation was applied successfully to Windsor geometry leading to results which were not expected prior to the experiments. This highlights the strength of optimisation techniques where trade-offs in vast design spaces are handled automatically and can be later studied to gain further insights into the resulting flow physics.

Chapter 6

Concluding remarks

As previously shown in the literature, realistic operating conditions can have an impact on the vehicle's aerodynamic efficiency. The work presented in this thesis is focused on wake aerodynamics, particularly at yaw. It also includes the development work of an optimisation method to facilitate the creation of low-drag reference geometry. The objective is to increase the knowledge of how vortical structures are related to the vehicles base pressure and in turn the vehicle efficiency, for side wind conditions.

The developed optimisation algorithm is a surrogate model-based technique using adaptively scaled Radial Basis Functions. Several benchmarks against other commonly used optimisation techniques showed good overall performance for both noise-free and noisy functions. Optimisation proved useful in this work with large design spaces and resulted in geometries which were not expected to perform the best prior to the test, highlighting the benefit of using optimisation methods in the creation of low-drag reference geometry.

The study of vehicle wakes at yaw revealed that improvements to the base pressure could be found by using a cavity in combination with a small "kick"-angle at the trailing edge of the cavity, modifying the bulk wake flow. Depending on the vehicle and cavity design, the kick angles ability to reduce drag varies. This indicates that the kick angles need to be optimised on a vehicle to vehicle basis.

Global changes to the wake balance could be achieved by manipulating the kick angle. Changes to the wakes unsteady behaviour due to the cavity and kick angle were also found; however, the influence on drag was not clear and it was not always the most stable wakes that reduce drag the most, something that other authors have also noted. The most reliable indicator of drag in the wake was the wake balance. By balancing the wake, i.e. angling the wake flow vectors to imping in the normal direction of the base, the largest improvements to drag were found. Based on this information, base drag reductions can be found efficiently by improving the wake balance.

6.1 Future work

The results from the study performed at Loughborough did not contain flow measurements as these were not available at the time of writing this thesis. Analysis

of the wake flow needs to be done to further understand the drag reduction mechanisms.

Unsteady flow control and devices aimed at reducing the unsteady contribution to drag have been applied successfully to ground vehicle geometries by other authors. These control strategies or devices often influence several aspects of the wake simultaneously when used in combination with often simplified geometries. It would be of interest to apply an active flow control method to a geometry that has been first optimised by manipulating the wake balance using fixed geometry and then applying an active control strategy to this geometry to investigate the additive effects of employing both strategies. This could be done at full scale with detailed geometry to measure the overall potential of such an approach whilst considering the power consumption of the flow control method.

Chapter 7

Summary of papers

7.1 Paper I

Numerical analysis of a vehicle wake with tapered rear extensions under yaw conditions The focus of the first paper is related to the objective of this thesis: to increase the knowledge of how vortical structures are related to the vehicles base pressure, especially at yaw and how it correlates to drag. A numerical investigation was performed of a fully detailed production vehicle with a tapered 3/4 cavity subject to side wind. The cavity protrudes 150 mm from the base and is investigated in two configurations: with a smooth taper and a taper with an added kick. A smooth taper provided the greatest drag improvement without side wind while the cavity with a kick yielded an additional reduction at yaw. This reduces the vehicle's sensitivity to side wind by improving the wake balance of the vehicle. Unsteady influences from the cavity were found; however, the most consistent indicator of the performance in relation to drag was the wake balance.

7.2 Paper II

Surrogate-based optimisation using adaptively scaled Radial Basis Functions

The second paper features method development of an optimisation algorithm that has been used in the yet unpublished work featured in Chapter 5. The performance of two surrogate-based optimisation methods; a Proper Orthogonal Decomposition-based method and a force-based method. The generic passenger vehicle DrivAer was used to investigate the surrogate model's predictive ability where the force based method outperformed the POD-based one. The surrogate model makes use of Radial Basis Function interpolation where the hyperparameters are optimised using differential evolution. An additional axis scaling factor was used and treated as hyperparameter reducing the interpolation error by more than 50 %. The performance of the force-based surrogate model was compared with three other gradient-free optimisation techniques showing as good, or better performance, for 16 out of the 18 tested benchmark problems.

Bibliography

[1] European Environment Agency. *Greenhouse gas emissions from transport*. 2018. URL: https://www.eea.europa.eu/data-and-maps/indicators/transport-emissions-of-greenhouse-gases/transport-emissions-of-greenhouse-gases-11 (visited on 03/19/2019).

[2] European Federation for Transport and Environment AISBL. *Mind the Gap 2016 - Report*. 2016. URL: https://www.transportenvironment.org/publications/mind-gap-2016-report (visited on 03/21/2019).

[3] Uwe Tietge et al. "FROM LABORATORY TO ROAD A 2015 update of official and "real-world" fuel consumption and CO2 values for passenger cars in Europe". In: (2015).

[4] Zifei Yang and Anup Bandivadekar. *2017 Global update: Light-duty vehicle greenhouse gas and fuel economy standards*. 2017. URL: https://www.theicct.org/publications/2017-global-update-LDV-GHG-FE-standards (visited on 03/20/2019).

[5] Jelica Pavlovic, Alessandro Marotta, and Biagio Ciuffo. "CO 2 emissions and energy demands of vehicles tested under the NEDC and the new WLTP type approval test procedures". en. In: *Applied Energy* 177 (Sept. 2016), pp. 661–670. ISSN: 03062619. DOI: 10.1016/j.apenergy.2016.05.110. URL: https://linkinghub.elsevier.com/retrieve/pii/S0306261916307152 (visited on 03/22/2019).

[6] J. Y. Wong. *Theory of ground vehicles*. en. 3rd ed. New York: John Wiley, 2001. ISBN: 978-0-471-35461-1.

[7] R. H. Barnard. *Road vehicle aerodynamic design : an introduction*. 3. ed. MechAero Pub., 2009. ISBN: 978-0-9540734-7-3.

[8] S. Windsor. "Real world drag coefficient – is it wind averaged drag?" en. In: *The International Vehicle Aerodynamics Conference*. Elsevier, 2014, pp. 3–17. ISBN: 978-0-08-100199-8. DOI: 10.1533/9780081002452.1.3. URL: https://linkinghub.elsevier.com/retrieve/pii/B9780081001998500010 (visited on 04/08/2019).

[9] Jeff Howell. "Aerodynamic Drag of Passenger Cars at Yaw". en. In: *SAE International Journal of Passenger Cars - Mechanical Systems* 8.1 (Apr. 2015). ISSN: 1946-4002. DOI: 10.4271/2015-01-1559. URL: http://papers.sae.org/2015-01-1559/ (visited on 03/01/2018).

[10] Thomas Christian Schuetz. *Aerodynamics of Road Vehicles, Fifth Edition*. English. 5 edition. Warrendale, Pennsylvania: SAE International, Dec. 2015. ISBN: 978-0-7680-7977-7.

[11] Adrian P. Gaylard et al. “Evaluation of Non-Uniform Upstream Flow Effects on Vehicle Aerodynamics”. en. In: *SAE International Journal of Passenger Cars - Mechanical Systems* 7.2 (Apr. 2014), pp. 692–702. ISSN: 1946-4002. DOI: 10.4271/2014-01-0614. URL: http://papers.sae.org/2014-01-0614/ (visited on 04/08/2019).

[12] Erik Josefsson et al. “Numerical Analysis of Aerodynamic Impact on Passenger Vehicles during Cornering”. In: May 2018. DOI: 10.4271/2018-37-0014. URL: http://www.sae.org/content/2018-37-0014/ (visited on 06/19/2018).

[13] Geoff Le Good et al. “Effects on the Aerodynamic Characteristics of Vehicles in Longitudinal Proximity Due to Changes in Style”. en. In: May 2018. DOI: 10.4271/2018-37-0018. URL: https://www.sae.org/content/2018-37-0018/ (visited on 04/08/2019).

[14] Joaquin Gargoloff et al. “Robust Optimization for Real World CO2 Reduction”. en. In: May 2018. DOI: 10.4271/2018-37-0015. URL: https://www.sae.org/content/2018-37-0015/ (visited on 04/08/2019).

[15] Tristan Favre. *Aerodynamics simulations of ground vehicles in unsteady crosswind*. en. OCLC: 940898583. Stockholm: KTH Royal Institute of Technology, 2011. URL: http://urn.kb.se/resolve?urn=urn:nbn:se:kth:diva-50242 (visited on 05/20/2019).

[16] Jeff Howell, David Forbes, and Martin Passmore. “A drag coefficient for application to the WLTP driving cycle”. en. In: *Proceedings of the Institution of Mechanical Engineers, Part D: Journal of Automobile Engineering* 231.9 (Aug. 2017), pp. 1274–1286. ISSN: 0954-4070, 2041-2991. DOI: 10.1177/0954407017704784. URL: http://journals.sagepub.com/doi/10.1177/0954407017704784 (visited on 03/01/2018).

[17] Max Varney, Martin Passmore, and Adrian Gaylard. “Parametric Study of Asymmetric Side Tapering in Constant Cross Wind Conditions”. In: Apr. 2018. DOI: 10.4271/2018-01-0718. URL: http://www.sae.org/content/2018-01-0718/ (visited on 04/24/2018).

[18] Wolf-Heinrich Hucho, ed. *Aerodynamics of Road Vehicles: From Fluid Mechanics to Vehicle Engineering*. 4 edition. Warrendale, PA: Society of Automotive Engineers Inc, Feb. 1998. 918 pp. ISBN: 978-0-7680-0029-0.

[19] Edward G. Duell and A. R. George. “Experimental Study of a Ground Vehicle Body Unsteady Near Wake”. In: *International Congress & Exposition*. SAE International, 1999. DOI: https://doi.org/10.4271/1999-01-0812. URL: https://doi.org/10.4271/1999-01-0812.

[20] Jeff Howell et al. “Bluff Body Drag Reduction with Ventilated Base Cavities”. In: *SAE International Journal of Passenger Cars - Mechanical Systems* 5.1 (Apr. 16, 2012), pp. 152–160. ISSN: 1946-4002. DOI: 10.4271/2012-01-0171. URL: http://papers.sae.org/2012-01-0171/ (visited on 12/02/2016).

[21] Kevin R. Cooper. "Truck Aerodynamics Reborn - Lessons from the Past". In: *International Truck & Bus Meeting & Exhibition*. SAE International, 2003. DOI: https://doi.org/10.4271/2003-01-3376. URL: https://doi.org/10.4271/2003-01-3376.

[22] Y.A. Irving Brown, S. Windsor, and A.P. Gaylard. "The Effect of Base Bleed and Rear Cavities on the Drag of an SUV". In: *SAE 2010 World Congress & Exhibition*. SAE International, 2010. DOI: https://doi.org/10.4271/2010-01-0512. URL: https://doi.org/10.4271/2010-01-0512.

[23] Anna-Kristina Perry, Giancarlo Pavia, and Martin Passmore. "Influence of short rear end tapers on the wake of a simplified square-back vehicle: wake topology and rear drag". In: *Experiments in Fluids* 57.11 (Nov. 1, 2016), p. 169. ISSN: 0723-4864, 1432-1114. DOI: 10.1007/s00348-016-2260-3. URL: http://link.springer.com/article/10.1007/s00348-016-2260-3 (visited on 11/30/2016).

[24] Jean-Luc Aider, Jean-François Beaudoin, and José Eduardo Wesfreid. "Drag and lift reduction of a 3D bluff-body using active vortex generators". en. In: *Experiments in Fluids* 48.5 (2010), pp. 771–789. ISSN: 0723-4864, 1432-1114. DOI: 10.1007/s00348-009-0770-y. URL: http://link.springer.com/10.1007/s00348-009-0770-y (visited on 06/20/2017).

[25] P. W. Bearman. "Investigation of the flow behind a two-dimensional model with a blunt trailing edge and fitted with splitter plates". en. In: *Journal of Fluid Mechanics* 21.02 (Feb. 1965), p. 241. ISSN: 0022-1120, 1469-7645. DOI: 10.1017/S0022112065000162. URL: http://www.journals.cambridge.org/abstract_S0022112065000162 (visited on 05/03/2019).

[26] Jonathan McNally et al. "Drag reduction on a flat-back ground vehicle with active flow control". In: *Journal of Wind Engineering and Industrial Aerodynamics* 145 (Oct. 1, 2015), pp. 292–303. ISSN: 0167-6105. DOI: 10.1016/j.jweia.2015.03.006. URL: http://www.sciencedirect.com/science/article/pii/S0167610515000665 (visited on 01/24/2018).

[27] Azeddine Kourta and Cédric Leclerc. "Characterization of synthetic jet actuation with application to Ahmed body wake". en. In: *Sensors and Actuators A: Physical* 192 (2013), pp. 13–26. ISSN: 09244247. DOI: 10.1016/j.sna.2012.12.008. URL: http://linkinghub.elsevier.com/retrieve/pii/S0924424712007364 (visited on 06/25/2017).

[28] Bae Geun Hwang et al. "Reduction of drag in heavy vehicles with two different types of advanced side skirts". In: *Journal of Wind Engineering and Industrial Aerodynamics* 155 (Aug. 1, 2016), pp. 36–46. ISSN: 0167-6105. DOI: 10.1016/j.jweia.2016.04.009. URL: http://www.sciencedirect.com/science/article/pii/S0167610515300416 (visited on 01/24/2018).

[29] Diogo Barros et al. "Bluff body drag manipulation using pulsed jets and Coanda effect". en. In: *Journal of Fluid Mechanics* 805 (Oct. 2016), pp. 422–459. ISSN: 0022-1120, 1469-7645. DOI: 10.1017/jfm.2016.508. URL: https://www.cambridge.org/core/journals/journal-of-fluid-mechanics/article/bluff-body-drag-manipulation-using-pulsed-jets-and-coanda-effect/12609816D2FF77F5372BA9B3E32F69A8 (visited on 11/29/2018).

[30] Giancarlo Pavia, Martin Passmore, and Max Varney. "Low-frequency wake dynamics for a square-back vehicle with side trailing edge tapers". en. In: *Journal of Wind Engineering and Industrial Aerodynamics* 184 (Jan. 2019), pp. 417–435. ISSN: 01676105. DOI: 10.1016/j.jweia.2018.12.009. URL: https://linkinghub.elsevier.com/retrieve/pii/S016761051830864X (visited on 02/14/2019).

[31] Sabine Bonitz. *Development of Separation Phenomena on a Passenger Car*. en. Chalmers University of Technology, 2018. ISBN: 978-91-7597-785-0. URL: https://research.chalmers.se/en/publication/510047 (visited on 05/04/2019).

[32] Anna K. Perry. "An investigation into the base pressure of simplified automotive squareback geometries". PhD thesis. Loughborough University, 2016. URL: https://dspace.lboro.ac.uk/2134/22605.

[33] S.R. Ahmed, G. Ramm, and G. Faltin. "Some Salient Features Of The Time-Averaged Ground Vehicle Wake". In: (1984). ISSN: 0148-7191. DOI: https://doi.org/10.4271/840300. URL: https://doi.org/10.4271/840300.

[34] Jeff Howell and Geoff Le Good. "The Effect of Backlight Aspect Ratio on Vortex and Base Drag for a Simple Car-Like Shape". In: Apr. 14, 2008. DOI: 10.4271/2008-01-0737. URL: http://papers.sae.org/2008-01-0737/ (visited on 01/04/2017).

[35] Lennert Sterken et al. "Wake and Unsteady Surface-Pressure Measurements on an SUV with Rear-End Extensions". In: *SAE Technical Papers*. Apr. 14, 2015. DOI: 10.4271/2015-01-1545. URL: http://papers.sae.org/2015-01-1545/ (visited on 11/30/2016).

[36] Simone Sebben, Lennert Sterken, and Thies Wölken. "Characterization of the rear wake of a sport utility vehicle with extensions and without extensions". In: *Institution of Mechanical Engineers, Part D: Journal of Automobile Engineering* (2016). DOI: DOI:10.1177/0954407016678016.

[37] Lennert Sterken et al. "Effect of Rear-End Extensions on the Aerodynamic Forces of an SUV". In: *SAE Technical Papers*. Apr. 1, 2014. DOI: 10.4271/2014-01-0602. URL: http://papers.sae.org/2014-01-0602/ (visited on 11/30/2016).

[38] Lars Davidson. "Large Eddy Simulations: How to evaluate resolution". In: *International Journal of Heat and Fluid Flow* 30.5 (2009). The 3rd International Conference on Heat Transfer and Fluid Flow in Microscale, pp. 1016–1025. ISSN: 0142-727X. DOI: https://doi.org/10.1016/j.ijheatfluidflow.2009.06.006. URL: http://www.sciencedirect.com/science/article/pii/S0142727X09001039.

[39] Grégoire Fourrié et al. "Bluff-body drag reduction using a deflector". In: *Experiments in Fluids* 50.2 (Feb. 2011), pp. 385–395. ISSN: 0723-4864, 1432-1114. DOI: 10.1007/s00348-010-0937-6. URL: http://link.springer.com/10.1007/s00348-010-0937-6 (visited on 06/27/2017).

[40] E Maskell. *Progress towards a method for the measurement of the components of the drag of a wing of finite span*. Royal Aircraft Establishment RAE, 1973.

[41] J. C. Wu. *A Generalized Wake-Integral Approach for Drag Determination in Three-Dimensional Flows*. 1979.

[42] G. Mccutcheon et al. "Wake Studies of a Model Passenger Car Using PIV". In: Dec. 2, 2002. DOI: 10.4271/2002-01-3335. URL: http://papers.sae.org/2002-01-3335/.

[43] S. R. Ahmed. "Wake structure of typical automobile shapes". In: *ASME J. Fluids Eng* 103 (1981), pp. 162–169. DOI: 10.1115/1.3240767. URL: http://fluidsengineering.asmedigitalcollection.asme.org/pdfaccess.ashx?ResourceID=4470551&PDFSource=13 (visited on 03/09/2017).

[44] M. Onorato, A.F. Costelli, and A. Garrone. "Drag Measurement Through Wake Analysis". In: Feb. 1, 1984. DOI: 10.4271/840302. URL: http://papers.sae.org/840302/ (visited on 12/07/2016).

[45] Antonello Cogotti. "A Strategy for Optimum Surveys of Passenger-Car Flow Fields". In: *SAE International Congress and Exposition*. SAE International, 1989. DOI: https://doi.org/10.4271/890374. URL: https://doi.org/10.4271/890374.

[46] P.W. Bearman. "Some Observations on Road Vehicle Wakes". In: *SAE International Congress and Exposition*. SAE International, 1984. DOI: https://doi.org/10.4271/840301. URL: https://doi.org/10.4271/840301.

[47] Alberto Morelli. "A New Aerodynamic Approach to Advanced Automobile Basic Shapes". In: *SAE 2000 World Congress*. SAE International, 2000. DOI: https://doi.org/10.4271/2000-01-0491. URL: https://doi.org/10.4271/2000-01-0491.

[48] Kunihiko Taira et al. "Modal Analysis of Fluid Flows: An Overview". In: *arXiv:1702.01453 [physics]* (Feb. 5, 2017). arXiv: 1702.01453. URL: http://arxiv.org/abs/1702.01453.

[49] Tomas W. Muld, Gunilla Efraimsson, and Dan S. Henningson. "Mode Decomposition on Surface-Mounted Cube". In: *Flow, Turbulence and Combustion* 88.3 (Apr. 2012), pp. 279–310. ISSN: 1386-6184, 1573-1987. DOI: 10.1007/s10494-011-9355-y. URL: http://link.springer.com/10.1007/s10494-011-9355-y (visited on 12/11/2017).

[50] Magnus Urquhart. *ProperOrthogonalDecomposition.jl - Release v0.1.0*. https://github.com/MrUrq/ProperOrthogonalDecomposition.jl. 2018.

[51] Anatol Roshko. *On the drag and shedding frequency of two-dimensional bluff bodies*. National Advisory Committee for Aeronautics; Washington, DC, United States, July 1, 1954. URL: http://ntrs.nasa.gov/search.jsp?R=19930083869 (visited on 04/20/2018).

[52] David E. Goldberg. *Genetic Algorithms in Search, Optimization and Machine Learning*. 1st. Boston, MA, USA: Addison-Wesley Longman Publishing Co., Inc., 1989. ISBN: 978-0-201-15767-3.

[53] Tushar Goel et al. "Ensemble of surrogates". en. In: *Structural and Multidisciplinary Optimization* 33.3 (Jan. 2007), pp. 199–216. ISSN: 1615-147X, 1615-1488. DOI: 10.1007/s00158-006-0051-9. URL: http://link.springer.com/10.1007/s00158-006-0051-9 (visited on 11/21/2018).

[54] Jiaqi Luo. "Design optimization of the last stage of a 4.5-stage compressor using a POD-based hybrid model". en. In: *Aerospace Science and Technology* 76 (May 2018), pp. 303–314. ISSN: 12709638. DOI: 10.1016/j.ast.2018.01.043. URL: http://linkinghub.elsevier.com/retrieve/pii/S1270963817312129 (visited on 03/02/2018).

[55] Emiliano Iuliano. "Global optimization of benchmark aerodynamic cases using physics-based surrogate models". en. In: *Aerospace Science and Technology* 67 (Aug. 2017), pp. 273–286. ISSN: 12709638. DOI: 10.1016/j.ast.2017.04.013. URL: http://linkinghub.elsevier.com/retrieve/pii/S1270963816312512 (visited on 03/02/2018).

[56] L Miretti et al. "Application of POD techniques in CFD optimization of vehicle aerodynamics". In: Coventry Transport Museum, Coventry, Sept. 2016.

[57] Valentina Dolci and Renzo Arina. "Proper Orthogonal Decomposition as Surrogate Model for Aerodynamic Optimization". en. In: *International Journal of Aerospace Engineering* 2016 (2016), pp. 1–15. ISSN: 1687-5966, 1687-5974. DOI: 10.1155/2016/8092824. URL: https://www.hindawi.com/journals/ijae/2016/8092824/ (visited on 03/02/2018).

[58] Emiliano Iuliano and Domenico Quagliarella. "Proper Orthogonal Decomposition, surrogate modelling and evolutionary optimization in aerodynamic design". In: *Computers & Fluids* 84 (Sept. 2013), pp. 327–350. ISSN: 0045-7930. DOI: 10.1016/j.compfluid.2013.06.007. URL: http://www.sciencedirect.com/science/article/pii/S0045793013002223.

[59] Angelina I. Heft, Thomas Indinger, and Nikolaus A. Adams. "Introduction of a New Realistic Generic Car Model for Aerodynamic Investigations". en. In: Apr. 2012. DOI: 10.4271/2012-01-0168. URL: http://papers.sae.org/2012-01-0168/ (visited on 11/08/2018).

[60] Stuart J. Bates, J Sienz, and Vassili Toropov. "Formulation of the Optimal Latin Hypercube Design of Experiments Using a Permutation Genetic Algorithm". In: 2011 (Apr. 2004). DOI: 10.2514/6.2004-2011.

[61] Shmuel Rippa. "An algorithm for selecting a good value for the parameter c in radial basis function interpolation". en. In: *Advances in Computational Mathematics* 11.2-3 (Nov. 1999), pp. 193–210. ISSN: 1019-7168, 1572-9044. DOI: 10.1023/A:1018975909870. URL: https://link.springer.com/article/10.1023/A:1018975909870 (visited on 05/02/2018).

[62] Gregory F. Fasshauer. *Meshfree Approximation Methods with MATLAB*. River Edge, NJ, USA: World Scientific Publishing Co., Inc., 2007. ISBN: 978-981-270-634-8.

[63] Kenneth P. Burnham, David Raymond Anderson, and Kenneth P. Burnham. *Model selection and multimodel inference: a practical information-theoretic approach*. en. 2nd ed. OCLC: ocm48557578. New York: Springer, 2002. ISBN: 978-0-387-95364-9.

[64] J. Bezanson et al. "Julia: A Fresh Approach to Numerical Computing". In: *SIAM Review* 59.1 (Jan. 2017), pp. 65–98. ISSN: 0036-1445. DOI: 10.1137/141000671. URL: https://epubs.siam.org/doi/10.1137/141000671 (visited on 10/03/2018).

[65] Magnus Urquhart. *LatinHypercubeSampling.jl - Release v1.2.0*. https://github.com/MrUrq/LatinHypercubeSampling.jl. 2018.

[66] Emil Ljungskog. *ScatteredInterpolation.jl - Release v0.3.0*. https://github.com/eljungsk/ScatteredInterpolation.jl. 2018.

[67] Robert Feldt. *BlackBoxOptim.jl - Release v0.4.0*. https://github.com/robertfeldt/BlackBoxOptim.jl. 2018.

[68] Patrick Kofod Mogensen and Asbjørn Nilsen Riseth. "Optim: A mathematical optimization package for Julia - Optim.jl release v0.17.2". In: *Journal of Open Source Software* 3.24 (2018), p. 615. DOI: 10.21105/joss.00615.

[69] Emil Ljungskog et al. "On the Effects of Wind Tunnel Floor Tangential Blowing on the Aerodynamic Forces of Passenger Vehicles". en. In: *SAE International Journal of Passenger Cars - Mechanical Systems* 10.2 (Mar. 2017). ISSN: 1946-4002. DOI: 10.4271/2017-01-1518. URL: http://papers.sae.org/2017-01-1518/ (visited on 06/25/2017).

[70] Stefan Jakobsson, Björn Andersson, and Fredrik Edelvik. "Rational radial basis function interpolation with applications to antenna design". In: *Journal of Computational and Applied Mathematics* 233.4 (Dec. 2009), pp. 889–904. ISSN: 0377-0427. DOI: 10.1016/j.cam.2009.08.058. URL: http://www.sciencedirect.com/science/article/pii/S0377042709004634 (visited on 10/04/2018).

[71] Scott A. Sarra and Yikun Bai. "A rational radial basis function method for accurately resolving discontinuities and steep gradients". en. In: *Applied Numerical Mathematics* 130 (Aug. 2018), pp. 131–142. ISSN: 01689274. DOI: 10.1016/j.apnum.2018.04.001. URL: https://linkinghub.elsevier.com/retrieve/pii/S0168927418300904 (visited on 11/27/2018).

[72] Jeff Howell, Martin Passmore, and Steve Windsor. "A Drag Coefficient for Test Cycle Application". en. In: *SAE International Journal of Passenger Cars - Mechanical Systems* 11.5 (Apr. 2018), pp. 447–461. ISSN: 1946-4002. DOI: 10.4271/2018-01-0742. URL: https://www.sae.org/content/2018-01-0742/ (visited on 04/12/2019).

[73] J. Marcos Garcia de la Cruz, Rowan D. Brackston, and Jonathan F. Morrison. "Adaptive Base-Flaps Under Variable Cross-Wind". en. In: Aug. 2017. DOI: 10.4271/2017-01-7000. URL: http://www.sae.org/content/2017-01-7000/ (visited on 10/02/2018).

[74] S.N. Skinner and H. Zare-Behtash. "State-of-the-art in aerodynamic shape optimisation methods". en. In: *Applied Soft Computing* 62 (Jan. 2018), pp. 933–962. ISSN: 15684946. DOI: 10.1016/j.asoc.2017.09.030. URL: https://linkinghub.elsevier.com/retrieve/pii/S1568494617305690 (visited on 09/20/2018).

[75] *Vehicle Aerodynamics Terminology (J1594 Ground Vehicle Standard) - SAE Mobilus*. URL: https://saemobilus.sae.org/content/j1594_199412 (visited on 05/21/2019).

[76] G. Johl. "The design and performance of a 1.9m x 1.3m indraft wind tunnel". PhD thesis. Loughborough University, 2010.

[77] Bahram Khalighi, Szabolcs R. Balkanyi, and Luis P. Bernal. "Experimental investigation of aerodynamic flow over a bluff body in ground proximity with drag reduction devices". In: *International Journal of Aerodynamics* 3.4 (2013), p. 217. ISSN: 1743-5447, 1743-5455. DOI: 10.1504/IJAD.2013.054421. URL: http://www.inderscience.com/link.php?id=54421 (visited on 12/02/2016).

[78] Mathieu Grandemange and Olivier Cadot. "A study of wake effects on the drag of the Ahmed's squareback model at the industrial scale". en. In: *Journal of Wind Engineering and Industrial Aerodynamics* (2015), p. 19.

Appendix A

Optimisation

A.1 Benchmark functions

Problem	Search space
f_1 Styblinski-Tang 2D	$x_i \in (-5.0, 5.0)$ for all i
f_2 Rastrigin 2D	$x_i \in (-5.12, 5.12)$ for all i
f_3 Rosenbrock 2D	$x_i \in (-5.0, 5.0)$ for all i
f_4 Beale 2D	$x_i \in (-4.5, 4.5)$ for all i
f_5 Sphere 2D	$x_i \in (-5.12, 5.12)$ for all i
f_6 Perm d, β 2D	$x_i \in (-2.0, 2.0)$ for all i
f_7 Goldstein-Price 2D	$x_i \in (-2.0, 2.0)$ for all i
f_8 Hartmann 6D	$x_i \in (0.0, 1.0)$ for all i
f_9 Rosenbrock 12D	$x_i \in (-5.0, 5.0)$ for all i

Table A.1: *Benchmark test function search space.*

Hartmann 6D coefficients

$$\alpha = \begin{pmatrix} 1.0 & 1.2 & 3.0 & 3.2 \end{pmatrix}$$

$$\mathbf{A} = \begin{pmatrix} 10 & 3 & 17 & 3.5 & 1.7 & 8 \\ 0.05 & 10 & 17 & 0.1 & 8 & 14 \\ 3 & 3.5 & 1.7 & 10 & 17 & 8 \\ 17 & 8 & 0.05 & 10 & 0.1 & 14 \end{pmatrix}$$

$$\mathbf{P} = 10^{-4} \begin{pmatrix} 1312 & 1696 & 5569 & 124 & 8283 & 5886 \\ 2329 & 4135 & 8307 & 3736 & 1004 & 9991 \\ 2348 & 1451 & 3522 & 2883 & 3047 & 6650 \\ 4047 & 8828 & 8732 & 5743 & 1091 & 381 \end{pmatrix}$$

Table A.2: *Hartmann 6D test function coefficients.*

A.2 Infill iterations

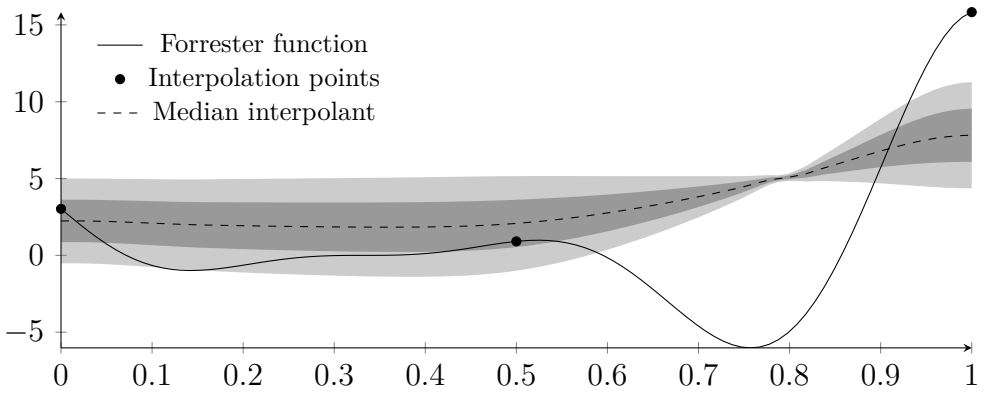

(a) *Three sampling points.*

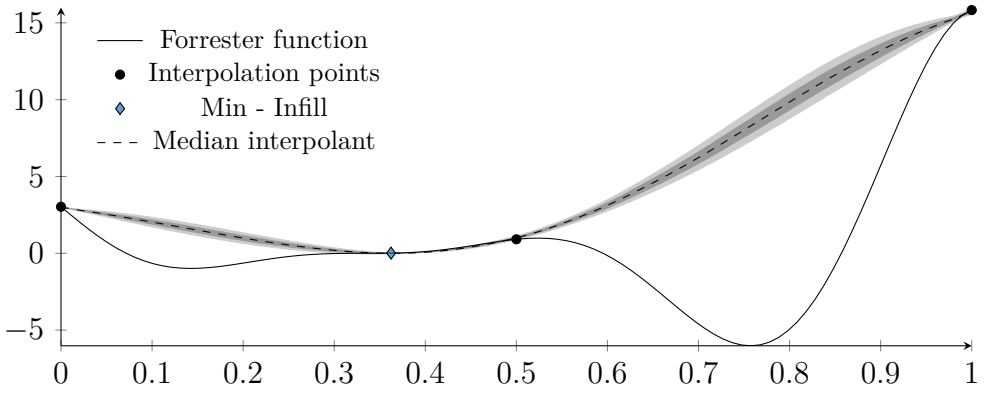

(b) *Three sampling points and one minimum infill point.*

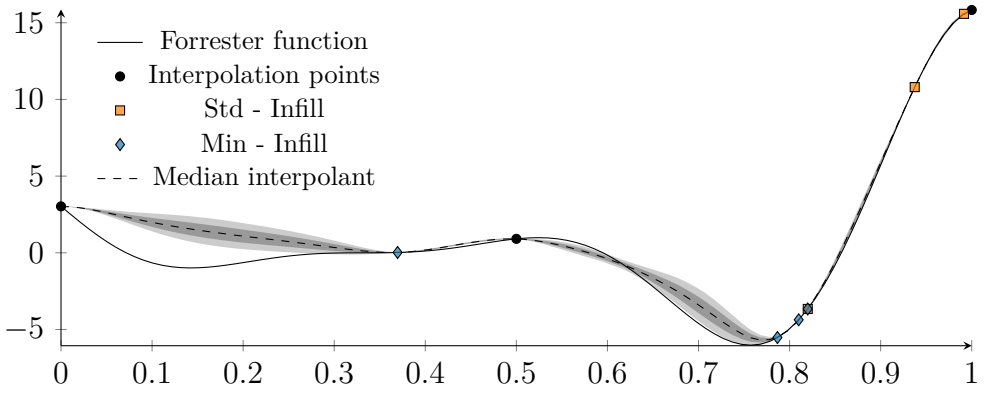

(c) *Three sampling points and seven infill points.*

Figure A.1: *Forrester function infill progression. The shaded areas represent the* ± 1 *and* ± 2 *standard deviation of the surrogate ensemble.*

A.3 Optimisation benchmark performance

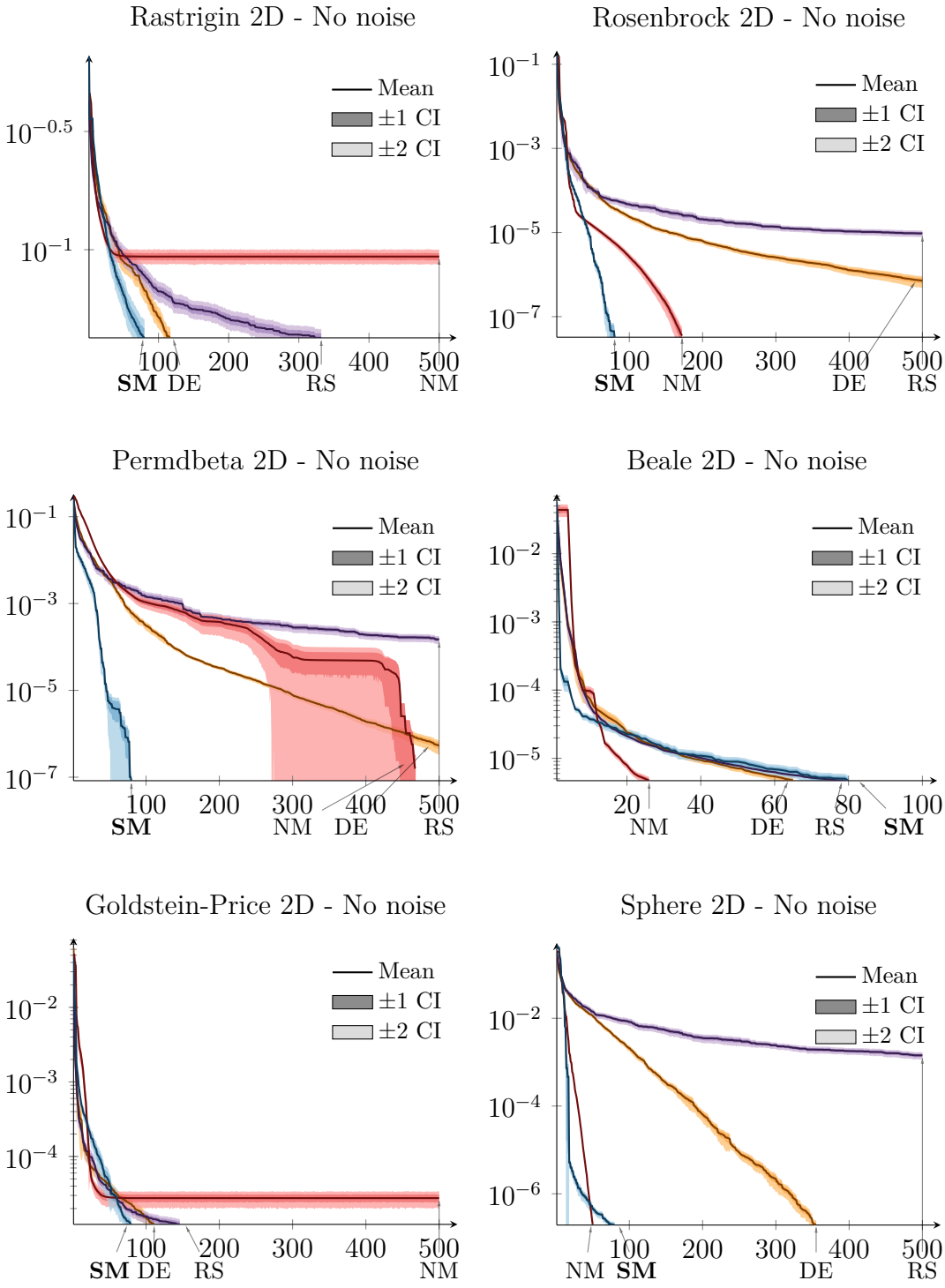

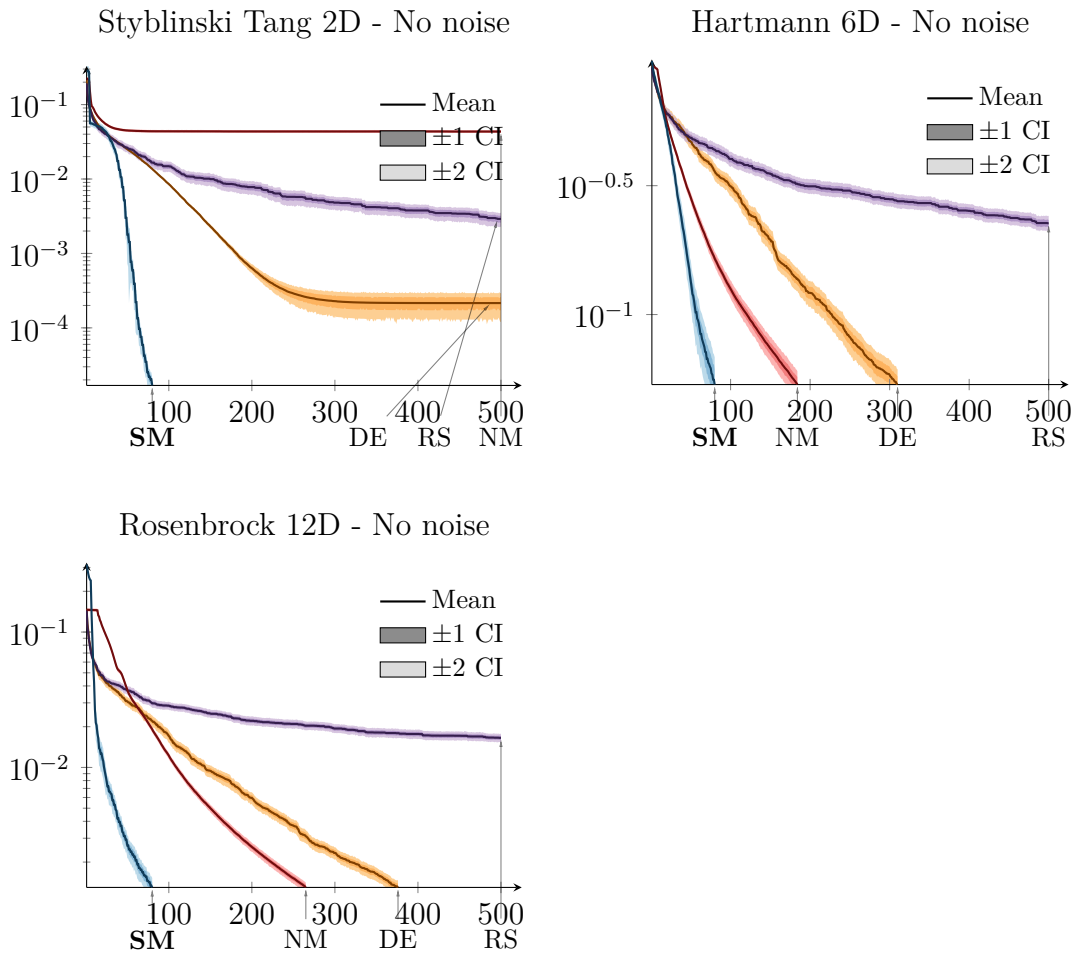

Figure A.2: *Optimisation benchmark performance, functions* f_{1-9}*. Results are normalized by the test function maximum and minimum value.*

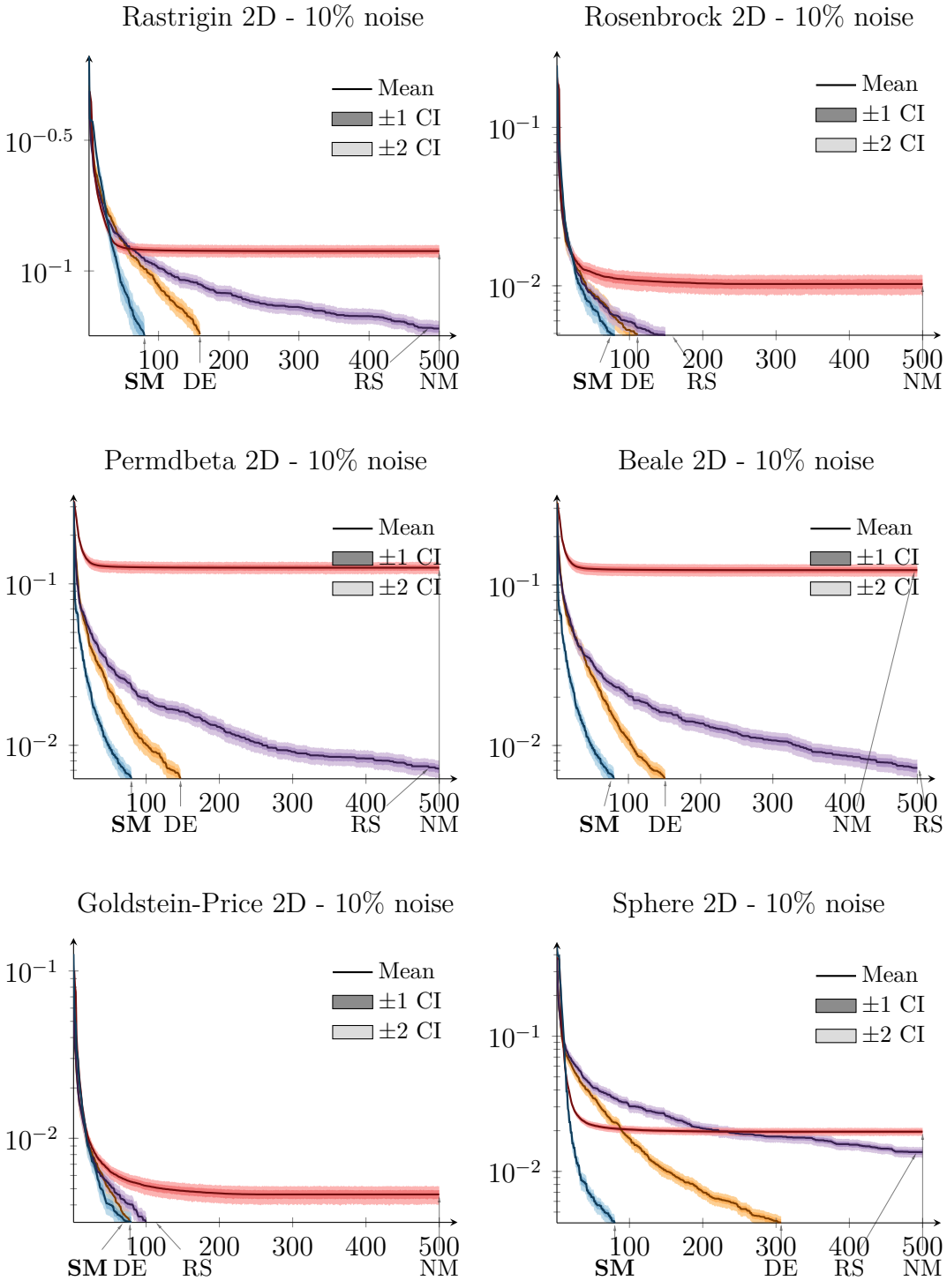
Rastrigin 2D - 10% noise
Mean
±1 CI
±2 CI
$10^{-0.5}$
10^{-1}
100
200
300
400
500
SM
DE
RS
NM
Rosenbrock 2D - 10% noise
Mean
±1 CI
±2 CI
10^{-1}
10^{-2}
100
200
300
400
500
SM
DE
RS
NM
Permdbeta 2D - 10% noise
Mean
±1 CI
±2 CI
10^{-1}
10^{-2}
100
200
300
400
500
SM
DE
RS
NM
Beale 2D - 10% noise
Mean
±1 CI
±2 CI
10^{-1}
10^{-2}
100
200
300
400
500
SM
DE
NM
RS
Goldstein-Price 2D - 10% noise
Mean
±1 CI
±2 CI
10^{-1}
10^{-2}
100
200
300
400
500
SM
DE
RS
NM
Sphere 2D - 10% noise
Mean
±1 CI
±2 CI
10^{-1}
10^{-2}
100
200
300
400
500
SM
DE
RS
NM

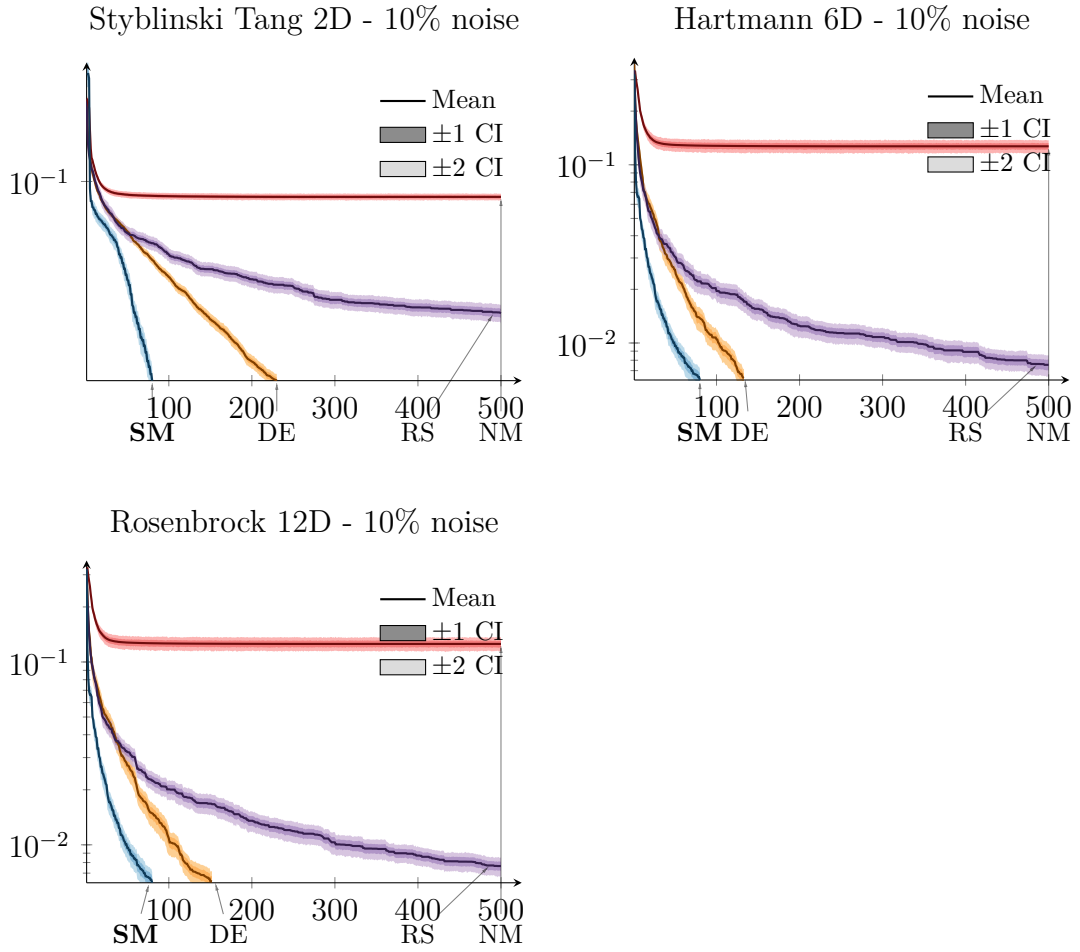

Figure A.3: *Optimisation benchmark performance, functions f_{1-9} with 10% white noise. Results are normalized by the test function maximum and minimum value.*